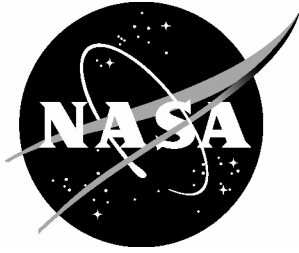NASA/TM–20220013891

A Dynamic Nonlinear Subgrid-Scale Model for Large-Eddy Simulation of Complex Turbulent Flows

Ali Uzun and Mujeeb R. Malik
Langley Research Center, Hampton, Virginia

NASA STI Program Report Series

Since its founding, NASA has been dedicated to the advancement of aeronautics and space science. The NASA scientific and technical information (STI) program plays a key part in helping NASA maintain this important role.

The NASA STI program operates under the auspices of the Agency Chief Information Officer. It collects, organizes, provides for archiving, and disseminates NASA's STI. The NASA STI program provides access to the NTRS Registered and its public interface, the NASA Technical Reports Server, thus providing one of the largest collections of aeronautical and space science STI in the world. Results are published in both non-NASA channels and by NASA in the NASA STI Report Series, which includes the following report types:

- TECHNICAL PUBLICATION. Reports of completed research or a major significant phase of research that present the results of NASA Programs and include extensive data or theoretical analysis. Includes compilations of significant scientific and technical data and information deemed to be of continuing reference value. NASA counterpart of peer-reviewed formal professional papers but has less stringent limitations on manuscript length and extent of graphic presentations.

- TECHNICAL MEMORANDUM. Scientific and technical findings that are preliminary or of specialized interest, e.g., quick release reports, working papers, and bibliographies that contain minimal annotation. Does not contain extensive analysis.

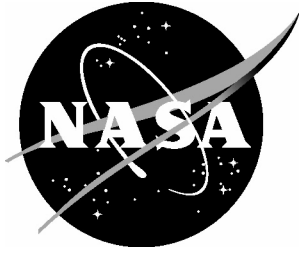- CONTRACTOR REPORT. Scientific and technical findings by NASA-sponsored contractors and grantees.

- CONFERENCE PUBLICATION. Collected papers from scientific and technical conferences, symposia, seminars, or other meetings sponsored or co-sponsored by NASA.

- SPECIAL PUBLICATION. Scientific, technical, or historical information from NASA programs, projects, and missions, often concerned with subjects having substantial public interest.

- TECHNICAL TRANSLATION. English-language translations of foreign scientific and technical material pertinent to NASA's mission.

Specialized services also include organizing and publishing research results, distributing specialized research announcements and feeds, providing information desk and personal search support, and enabling data exchange services.

For more information about the NASA STI program, see the following:

- Access the NASA STI program home page at http://www.sti.nasa.gov

- Help desk contact information:

https://www.sti.nasa.gov/sti-contact-form/
and select the "General" help request type.

NASA/TM–20220013891

A Dynamic Nonlinear Subgrid-Scale Model for Large-Eddy Simulation of Complex Turbulent Flows

Ali Uzun and Mujeeb R. Malik
Langley Research Center, Hampton, Virginia

October 2022

A Dynamic Nonlinear Subgrid-Scale Model for Large-Eddy Simulation of Complex Turbulent Flows

Ali Uzun

National Institute of Aerospace, Hampton, Virginia 23666

Mujeeb R. Malik

NASA Langley Research Center, Hampton, Virginia 23681

Abstract

We present a new dynamic nonlinear subgrid-scale (SGS) model for large-eddy simulations (LES) and apply it to compute a flow involving pressure gradients, surface curvature and separation, for which data from a direct numerical simulation are available for comparison. The model, inspired by the triple model idea of Bardina et al. ("Improved Turbulence Models Based on Large Eddy Simulation of Homogeneous, Incompressible, Turbulent Flows," Report No. TF-19, Thermosciences Division, Department of Mechanical Engineering, Stanford University, 1983), includes a Galilean-invariant term called the modified Leonard stress tensor, and two nonlinear terms comprised of the products of the strain-rate and rotation-rate tensors for an improved representation of the subgrid-scale dissipation, backscatter and anisotropy effects. The model does not employ any ad hoc averaging or clipping procedures, and does not require the specification of a characteristic length scale; hence, it naturally avoids the ambiguities associated with defining a proper length scale for anisotropic grids. Results from the wall-resolved LES of flow past a Gaussian bump using the new model demonstrate improved prediction of skin-friction, flow separation, mean flow profiles and turbulent quantities when compared to implicit LES as well as explicit LES using the Vreman SGS model on the same grid.

1 Introduction

Ongoing computational investigations of the so-called "speed bump" flow [1], which is a new benchmark smooth-body flow separation problem that involves strong acceleration of a turbulent boundary layer followed by separation due to adverse pressure gradient around a wall-mounted Gaussian bump, have shown that this new test case is quite challenging to predict by scale-resolving simulations performed in the form of wall-modeled large-eddy simulation (WMLES) [2, 3]*, [4], and wall-resolved large-eddy simulation (WRLES)[†]. The complex interaction of the incoming turbulent boundary layer with the strong favorable and adverse pressure gradients generated by the Gaussian bump, in addition to the surface curvature-induced effects, presents unique difficulties for the wall models and the subgrid-scale (SGS) models used in LES. The recent hybrid Direct Numerical Simulation (DNS) – WRLES of Uzun and Malik [5] performed for a spanwise-periodic configuration[‡] of the problem revealed that a thin internal layer is generated beneath the original turbulent boundary layer as the flow accelerates over the windward side of the bump, which then evolves into a free shear layer that develops in the deceleration region over the leeward side and subsequently separates. The internal layer is believed to be initiated by the change from the mild adverse to

---

*The shortcomings of the Reynolds-averaged Navier-Stokes (RANS) calculations for the speed bump flow can also be found in these two WMLES studies.

[†]The unsatisfactory WRLES performance observation is based on our own unpublished studies for the speed bump flow.

[‡]This simulation was performed using a total of 10.2 billion points, for a Reynolds number of $Re_L = 2$ million (bump height Reynolds number of 170000), with a domain span of $0.08L$, where L is the width of the experimental model.

1

strong favorable pressure gradient at the foot of the bump. Strong peaks in all Reynolds stress components emerge within the internal layer as it grows in the acceleration region. Furthermore, significant anisotropy in the normal Reynolds stresses, along both the wall-normal and streamwise directions, was found in the acceleration region. The flow interaction with the pressure gradient and surface curvature effects in the same region also forces the ratio between the Reynolds shear stress and the turbulent kinetic energy to significantly deviate from its known behavior under zero pressure gradient and no curvature conditions.

In the meantime, accompanying experimental investigations of the problem at hand, conducted by Williams et al. [6, 7] and Gray et al. [8, 9], have provided some validation data for the computational efforts, with additional measurements expected in the near future. Due to the limited nature of the experimental measurements at the time of this writing, the assessment of lower-fidelity RANS and WMLES calculations [2, 3, 4] for the spanwise-periodic configuration has been mostly performed via comparison with the corresponding data from the hybrid DNS – WRLES of Uzun and Malik [5]. For brevity, this simulation will be referred to as the DNS (in a loose sense) from hereon. It is also worth mentioning that this high-fidelity simulation was performed prior to the experiment of Gray et al. [8, 9], and their measured skin-friction along the centerline of the bump agreed quite well with the DNS results. This mutual validation between the simulation results and the experimental measurements provides additional confidence in both datasets. Thus, the available DNS dataset serves as a useful tool for the evaluation of the various SGS models considered during the course of the present study.

To investigate whether results comparable to those from the DNS [5] can be obtained at a significantly reduced computational cost, we recently embarked on a study to search for a robust SGS model that can be used to perform the best possible WRLES for the same spanwise-periodic configuration as in Uzun and Malik [5], on a grid that was coarsened by a factor of four both along the streamwise and spanwise directions. The grid resolution along the wall-normal direction was left unchanged. Somewhat unsurprisingly, the first WRLES on this coarsened grid did not yield satisfactory predictions when the implicit LES (ILES) approach (i.e., no explicit SGS model) was employed since the chosen grid coarsening was already known to be a bit too extreme for the ILES to produce a reliable result. As will be seen, an explicit LES based on the popular Vreman SGS model [10] on the same grid did not lead to any improved results either. In contrast, we had previously found the Vreman model to produce acceptable results in the case of the NASA wall-mounted hump flow [11], and in our unpublished studies of the periodic-hill flow problem [12]. This observation once again shows that a particular model that works reasonably well in a given test case may not perform satisfactorily in a different test case involving similar physical phenomena. The poor performance of ILES as well as explicit LES using the Vreman SGS model, which is a linear eddy-viscosity type model, then led us to try some of the nonlinear SGS models available in the literature. Simulations performed with the currently available nonlinear models also proved to be not completely satisfactory, which provided us with the motivation to develop an improved nonlinear SGS model that attempts to combine the best features of some of the existing modeling approaches.

A detailed review of all nonlinear SGS models to date is beyond the scope of the present work. Instead, we shall briefly describe the prior relevant work instrumental to the development of the present nonlinear model and establish the connection between the present and previous models. To our knowledge, Bardina et al. [13] were the first proponents of a nonlinear model for LES. In their study, they proposed and evaluated a "triple model," which was a linear combination of their own scale-similarity model, the well-known Smagorinsky linear eddy-viscosity model, and an additional nonlinear term comprised of the tensor contractions between the strain-rate tensor and the rotation-rate tensor. This nonlinear term was attributed to the earlier work of Wilcox and Rubesin [14] in the context of RANS turbulence models. The original scale-similarity model of Bardina et al. [13] is capable of generating both dissipation and backscatter, however, the net dissipation of the model was found to be insufficient. Hence, an eddy-viscosity term had to be added to the scale-similarity part in order for the model to generate sufficient net dissipation. The additional nonlinear term included in the triple model does not generate dissipation or backscatter (because the contraction

of this term with the strain-rate tensor is zero), but accounts for anisotropy effects. Using the available DNS data at the time, Bardina et al. [13] evaluated the correlation coefficients between the "exact" and triple model values of the SGS stresses for homogeneous isotropic and sheared turbulence, and observed a high degree of correlation. Despite this promising success of the proposed triple model demonstrated in an a priori manner in the early 1980s, no follow-up work on this model in more complex flows appears to have been performed in the subsequent years.

Beginning in the 1990s, an alternative nonlinear model of the following general form was investigated by several researchers [15]§, [16, 17, 18, 19]

$$\tau_{ij}^d = -2\mu_t \left(\widetilde{S}_{ij} - \frac{\delta_{ij}}{3} \widetilde{S}_{kk} \right) + \overline{\rho} C_1 \overline{\Delta}^2 \left(\widetilde{S}_{ik} \widetilde{S}_{kj} - \frac{\delta_{ij}}{3} \widetilde{S}_{kl} \widetilde{S}_{kl} \right) + \overline{\rho} C_2 \overline{\Delta}^2 \left(\widetilde{S}_{ik} \widetilde{\Omega}_{kj} - \widetilde{\Omega}_{ik} \widetilde{S}_{kj} \right) \tag{1}$$

where τ_{ij}^d is the deviatoric part of the SGS stress tensor, δ_{ij} is the Kronecker delta, μ_t is the eddy viscosity that can be computed using various models, $\overline{\rho}$ is the resolved density, $\widetilde{S}_{ij}$ and $\widetilde{\Omega}_{ij}$ are the resolved strain-rate and rotation-rate tensors, respectively, $\overline{\Delta}$ is the characteristic length scale, and C_1 and C_2 are the nonlinear model coefficients. The origin of the above model can be traced back to a general nonlinear constitutive relation derived for RANS modeling [20]. Equation (1) is essentially the reduced version of a more sophisticated constitutive relation. The first term on the right-hand side is the familiar linear eddy-viscosity term, which is responsible for generating the SGS dissipation, assuming a positive μ_t. The second term on the right is the nonlinear term that generates energy transfer from the subgrid scales to the resolved scales (also known as backscatter) when C_1 has a negative value; conversely, the term generates energy transfer from the resolved scales to the subgrid scales, or SGS dissipation, with a positive C_1. The third term on the right is the same as the nonlinear term used in the triple model of Bardina et al. [13] and accounts for anisotropy effects.

Kosović [16] proposed a constant coefficient version of the above model with $C_1 = C_2 < 0$ based on a theoretical analysis of isotropic turbulence and heuristic arguments. The coefficient value was made dependent upon an assumed backscatter parameter. Using stochastic analysis, Heinz [17] derived an alternative version of the above general model with $C_1 = -2C_2$, while Heinz and Gopalan [18] proposed a localized dynamic procedure to determine the nonlinear term coefficient in Ref. [17] along with the coefficient for the eddy viscosity. Wang and Bergstrom [19] proposed another localized dynamic technique for the determination of the three coefficients that appear in Eq. (1) (C_1, C_2 and the coefficient needed for μ_t). Heinz and Gopalan [18] showed that their formulation and the alternative version of Wang and Bergstrom [19] produced very similar results for the turbulent channel flow problem.

Despite the promising success of the nonlinear model given by Eq. (1) in the aforementioned references, our initial investigations of the speed bump problem using variations of this nonlinear formulation, with the eddy viscosity computed using several available models, did not produce results that were more accurate than those obtained with the proposed model. Thus, for brevity, those less accurate results are omitted in this document. We are unaware of any successful application of the model shown in Eq. (1) to a smooth-body flow separation test case similar to the speed bump flow. It is worth noting that Rasam et al. [21] also developed an alternative nonlinear model similar to that in Eq. (1), except that the second term on the right-hand side was removed, and the model formulation was revised to incorporate the SGS kinetic energy as a multiplying factor for both the linear and the nonlinear terms. This particular nonlinear model showed good success in the periodic-hill flow test case; however, its main drawback in our opinion is that it requires the specification of four constant coefficients before the fifth model coefficient is dynamically computed. Such an approach did not appear as an attractive option and hence was not considered in our investigations. Our work therefore focused on formulating an improved nonlinear model that combines the best features

---

§This study also considered more sophisticated versions with additional nonlinear terms involving products of the strain-rate and rotation-rate tensors in a priori evaluations of the various formulations.

of the original triple model of Bardina et al. [13] and the alternative model given in Eq. (1), with some additional modifications as described below.

2 SGS Model Details

For compressible flows, the flowfield variables are expressed in terms of Favre-filtered quantities [22]. A Favre-filtered quantity is defined as $\tilde{f} = \overline{\rho f}/\overline{\rho}$, where ρ is the fluid density, f is the unfiltered variable, $\tilde{f}$ is the Favre-filtered variable, and the overline denotes a spatial filtering operation. The governing equations to be solved for the evolution of the compressible flow are formulated in terms of the Favre-filtered flow variables. The corresponding SGS stress tensor that appears in the governing equations is given by

$$\tau_{ij} = \overline{\rho u_i u_j} - \frac{\overline{\rho u_i}\,\overline{\rho u_j}}{\overline{\rho}} = \overline{\rho}\left(\widetilde{u_i u_j} - \tilde{u}_i \tilde{u}_j\right) \tag{2}$$

where $\overline{(\ )}$ now denotes the implicit grid filter imposed by the application of the numerical discretization scheme on a local grid resolution of Δ, $\widetilde{(\ )}$ is the corresponding Favre filter, and u_i is the unfiltered velocity component.

We propose a model of the following form

$$\tau_{ij} - \frac{2}{3}\overline{\rho}k_{sgs}\delta_{ij} = C_1 \frac{\overline{\rho}k_{sgs}}{L_{kk}^m}\left(L_{ij}^m - \frac{\delta_{ij}}{3}L_{kk}^m\right) + C_2 \frac{\overline{\rho}k_{sgs}}{|\widetilde{M}|}\widetilde{M}_{ij} + C_3 \frac{\overline{\rho}k_{sgs}}{|\widetilde{N}|}\widetilde{N}_{ij}\,, \tag{3}$$

where

$$L_{ij}^m = \widehat{\overline{\rho}\tilde{u}_i \tilde{u}_j} - \frac{\widehat{\overline{\rho}\tilde{u}_i}\,\widehat{\overline{\rho}\tilde{u}_j}}{\widehat{\overline{\rho}}} \tag{4}$$

is the compressible version of the so-called modified Leonard stress tensor, which is Galilean invariant [23, 24], as are the other terms of the model, and $\widehat{(\ )}$ indicates spatial filtering at a scale that is greater than the grid filter width. The grid filter width is taken as $\ell\Delta$, where Δ is the local grid spacing[¶] and the value of ℓ depends upon the details of the underlying numerical discretization scheme. Typically, either $\ell = 1$ or 2 is used [25] without a rigorous justification. A value of $\ell = 1$ would be appropriate only for spectral schemes, while $\ell > 1$ or possibly $\ell > 2$ is necessary for other schemes. As will be discussed, for the high-order compact finite-difference scheme used in the present flow solver, the maximum resolvable wavenumber based on a stringent error criterion for the dispersive characteristics of the scheme [26] gives $\ell = 1.7$. For a standard second-order scheme, the same criterion would yield $\ell \approx 31$, which is obviously impractical. Hence, an alternative criterion would be needed to determine a more reasonable ℓ for lower-order schemes. That matter is not our main concern but is noted here as an open question. In our case, we shall use $\ell = 1.7$, as determined from the error criterion. The width corresponding to the $\widehat{(\ )}$ filtering operation in Eq. (3) is $m\Delta$, where $m > \ell$. The model coefficients C_1, C_2, C_3 are determined using a localized dynamic procedure, which requires test-filtering of the resolved flowfield with two separate filter widths greater than $\ell\Delta$, the details of which will be discussed later. The SGS kinetic energy, $k_{sgs} = 0.5\tau_{kk}/\overline{\rho}$, appearing in Eq. (3) is obtained from the solution of a transport equation to be introduced. The tensors $\widetilde{M}_{ij}$ and $\widetilde{N}_{ij}$ in Eq. (3) are defined as

$$\widetilde{M}_{ij} = \widetilde{S}_{ik}\widetilde{S}_{kj} - \frac{\delta_{ij}}{3}\widetilde{S}_{kl}\widetilde{S}_{kl}\,, \quad \widetilde{N}_{ij} = \widetilde{S}_{ik}\widetilde{\Omega}_{kj} - \widetilde{\Omega}_{ik}\widetilde{S}_{kj}\,, \tag{5}$$

[¶]For anisotropic grid spacings, Δ (not to be confused with the characteristic length scale, $\overline{\Delta}$) can be defined separately for each spatial direction as Δ_i, thereby giving a respective grid filter width for each direction. The following discussion will refer to Δ rather than Δ_i without any loss of generality.

with $|\widetilde{M}| = \left(\widetilde{M}_{ij}\widetilde{M}_{ij}\right)^{1/2}$, $|\widetilde{N}| = \left(\widetilde{N}_{ij}\widetilde{N}_{ij}\right)^{1/2}$. $\widetilde{S}_{ij}$ and $\widetilde{\Omega}_{ij}$ are the resolved strain-rate and rotation-rate tensors, respectively, given by

$$\widetilde{S}_{ij} = \frac{1}{2}\left(\frac{\partial \tilde{u}_i}{\partial x_j} + \frac{\partial \tilde{u}_j}{\partial x_i}\right), \quad \widetilde{\Omega}_{ij} = \frac{1}{2}\left(\frac{\partial \tilde{u}_i}{\partial x_j} - \frac{\partial \tilde{u}_j}{\partial x_i}\right). \tag{6}$$

Note that in the above tensor expressions, the tilde symbol over a tensor is meant to indicate that the tensor is based on the spatial derivatives of the Favre-filtered velocity components.

Unlike Eq. (1), there is no characteristic length scale appearing in the second and third terms on the right-hand side of Eq. (3). Instead, those terms contain $\bar{\rho}k_{sgs}$ and are normalized by either $|\widetilde{M}|$ or $|\widetilde{N}|$ for dimensional consistency$^{\parallel}$. We choose not to use any length scale in our model formulation because the matter of defining the most appropriate length scale for anisotropic grids is far from being resolved. For example, in a recent study by Schumann et al. [27], several different length scales, including the most commonly-used cubic-root of the cell volume as well as the local maximum grid spacing, among other choices, were considered in the LES of turbulent channel flows. It was found that while some length scales performed better than others, none produced results independent of the grid anisotropy. Furthermore, a particularly disturbing observation showed that every model and length scale tested in that study produced accurate results on at least one grid and inaccurate results on at least one other grid. Given these unresolved issues, a model that is free of any length scales in its formulation, as in Eq. (3), seems a reasonable choice.

The first term on the right-hand side of Eq. (3) owes its origin to the scale-similarity model proposed by Bardina et al. [13]. To provide some more background about this term, it is useful to consider the following conventional decomposition of τ_{ij} for an incompressible flow. Without any loss of generality,

$$\tau_{ij} = \overline{u_i u_j} - \overline{u}_i\overline{u}_j = \mathscr{L}_{ij} + \mathscr{C}_{ij} + \mathscr{R}_{ij} \tag{7}$$

where

$$\mathscr{L}_{ij} = \overline{\overline{u}_i\overline{u}_j} - \overline{u}_i\overline{u}_j, \quad \mathscr{C}_{ij} = \overline{\overline{u}_i u'_j} + \overline{u'_i\overline{u}_j}, \quad \mathscr{R}_{ij} = \overline{u'_i u'_j}, \quad u'_i = u_i - \overline{u}_i. \tag{8}$$

$\mathscr{L}_{ij}, \mathscr{C}_{ij}$ and $\mathscr{R}_{ij}$ are commonly referred to as the Leonard stress, cross-stress and the true SGS Reynolds stress tensors, respectively. The scale-similarity assumption of Bardina et al. [13] leads to $\overline{\overline{u}_i u'_j} \approx \overline{\overline{u}}_i\, \overline{u'_j}$ and $\overline{u'_i u'_j} \approx \overline{u'_i}\,\overline{u'_j}$. We can therefore write

$$\mathscr{C}_{ij} = \overline{\overline{u}_i u'_j} + \overline{u'_i\overline{u}_j} \approx \overline{\overline{u}}_i\, \overline{u'_j} + \overline{u'_i}\,\overline{\overline{u}}_j = \overline{\overline{u}}_i\left(\overline{u}_j - \overline{\overline{u}}_j\right) + \left(\overline{u}_i - \overline{\overline{u}}_i\right)\overline{\overline{u}}_j \tag{9}$$

and

$$\mathscr{R}_{ij} = \overline{u'_i u'_j} \approx \overline{u'_i}\,\overline{u'_j} = \left(\overline{u}_i - \overline{\overline{u}}_i\right)\left(\overline{u}_j - \overline{\overline{u}}_j\right). \tag{10}$$

Adding the three components with the above approximations gives

$$\mathscr{L}_{ij} + \mathscr{C}_{ij} + \mathscr{R}_{ij} \approx \mathscr{L}^m_{ij} = \overline{\overline{u}_i\overline{u}_j} - \overline{\overline{u}}_i\overline{\overline{u}}_j \tag{11}$$

where $\mathscr{L}^m_{ij}$ is the modified Leonard tensor in the case of an incompressible flow. $\mathscr{L}^m_{ij}$ is an *approximation* to the SGS stress tensor that can be computed using the information available from the resolved velocity field. The analogous expression of the modified Leonard tensor for a compressible flow is given in Eq. (4). The width of the spatial filtering operation needed to evaluate the modified Leonard tensor can normally be taken as equal to or greater than the local grid filter width. However, the numerical resolution in the immediate vicinity of the grid filter width can be considered marginal at best; hence, filtering with a larger width would

---

$^{\parallel}$Note that either or both denominators may become zero in case a uniform inviscid or an irrotational region were to exist in the immediate vicinity of the turbulent flow under investigation, but such a scenario is unlikely in the problems for which the present model is intended. A very small number may be added to the denominator to avoid division by zero if necessary.

allow the extraction of information from the better-resolved length scales of the flowfield. We therefore opt to use a larger filter width for the evaluation of the modified Leonard tensor in our model.

As noted above, the modified Leonard tensor is an approximation to the SGS stress tensor, and is evaluated using a spatial filter width greater than the local grid spacing. Our model contains additional terms to provide corrections for an improved representation of the SGS stress tensor. Under such conditions, the use of a coefficient for the scale-similarity term is appropriate and does not create any inconsistency as the term is Galilean invariant. The quantities to be filtered for the evaluation of L_{ij}^m are constructed from the resolved flowfield. Similarly, the tensors appearing in the second and third terms on the right-hand side of Eq. (3) are evaluated using the readily-available resolved velocity field. The proposed model does not include a linear eddy-viscosity term, as our experience indicates including such a term leads to a degradation of the solution accuracy for the present test case. Nevertheless, the second term of the proposed model plays a similar role to that of a linear eddy-viscosity term, and is capable of generating dissipation or backscatter, depending on the sign of its coefficient.

Our model can be viewed as a modified version of the original triple model of Bardina et al. [13]. The scale-similarity term of the original triple model is of the form

$$R_{ij} = C_B \left(\overline{\overline{u}_i \overline{u}_j} - \overline{\overline{\overline{u}}_i \overline{\overline{u}}_j} - \frac{\delta_{ij}}{3} \left(\overline{\overline{u}_k \overline{u}_k} - \overline{\overline{\overline{u}}_k \overline{\overline{u}}_k} \right) \right) \tag{12}$$

with the constant C_B set to 1.1**. This formulation results from using only the $\mathscr{C}_{ij}$ and $\mathscr{R}_{ij}$ approximations given above in the SGS stress tensor representation and omitting $\mathscr{L}_{ij}$, which is directly computed without approximations and included in the governing equations separately. Speziale [28] showed that C_B must be set to 1 for this particular formulation to be Galilean invariant. The above term is replaced by the Galilean-invariant modified Leonard tensor with a dynamic coefficient in the current model. Our scale-similarity term additionally includes the nondimensional scaling factor of $\left(\overline{\rho} k_{sgs} / L_{kk}^m \right)$ so that it naturally vanishes as k_{sgs} approaches zero, as do the other terms of the model. The filtering operation in the above Bardina et al. term is performed at the grid filter width, whereas a larger filter width is used in our case for the reason given earlier. To reiterate, our model also removes the linear eddy-viscosity term of the original triple model and replaces it with the second term of the alternative model from Eq. (1).

To derive an equation that can be used to compute the model coefficients, we first assume that the constitutive relationship given in Eq. (3) for subgrid scales is also valid at larger scales, which are several times the size of the largest subgrid scales. We can therefore write the following relationship, which has the same structure as Eq. (3) with the same coefficients

$$T_{ij} - \frac{\delta_{ij}}{3} T_{kk} = C_1 \frac{0.5 T_{kk}}{H_{kk}} \left(H_{ij} - \frac{\delta_{ij}}{3} H_{kk} \right) + C_2 \frac{0.5 T_{kk}}{|\widehat{M}|} \widehat{M}_{ij} + C_3 \frac{0.5 T_{kk}}{|\widehat{N}|} \widehat{N}_{ij} , \tag{13}$$

where

$$T_{ij} = \widehat{\rho u_i u_j} - \frac{\widehat{\rho u_i}\,\widehat{\rho u_j}}{\widehat{\rho}} , \quad H_{ij} = \widetilde{\widehat{\rho} \hat{u}_i \hat{u}_j} - \frac{\widetilde{\widehat{\rho} \hat{u}_i}\,\widetilde{\widehat{\rho} \hat{u}_j}}{\widetilde{\widehat{\rho}}} , \quad \hat{u}_i = \frac{\widehat{\rho u_i}}{\widehat{\rho}} , \tag{14}$$

$$\widehat{M}_{ij} = \widehat{S}_{ik}\widehat{S}_{kj} - \frac{\delta_{ij}}{3}\widehat{S}_{kl}\widehat{S}_{kl} , \quad \widehat{N}_{ij} = \widehat{S}_{ik}\widehat{\Omega}_{kj} - \widehat{\Omega}_{ik}\widehat{S}_{kj} , \quad |\widehat{M}| = \left(\widehat{M}_{ij}\widehat{M}_{ij} \right)^{1/2} , \quad |\widehat{N}| = \left(\widehat{N}_{ij}\widehat{N}_{ij} \right)^{1/2} , \tag{15}$$

$$\widehat{S}_{ij} = \frac{1}{2}\left(\frac{\partial \hat{u}_i}{\partial x_j} + \frac{\partial \hat{u}_j}{\partial x_i} \right) , \quad \widehat{\Omega}_{ij} = \frac{1}{2}\left(\frac{\partial \hat{u}_i}{\partial x_j} - \frac{\partial \hat{u}_j}{\partial x_i} \right) . \tag{16}$$

**This value and the constant coefficients of the other terms in their model were determined by correlating the model predictions with the available DNS data of homogeneous isotropic and sheared turbulence.

In the above formulation, the filtering operation denoted by $\widehat{(\ )}$ has a width of $m\Delta$, which is the same as that in Eq. (3), while the second filtering operation denoted by $\widetilde{(\ )}$ has a larger width, $n\Delta$, where $n > m$. The scale-invariance assumption employed here implies that the ratio between the filter widths of H_{ij} and T_{ij} in Eq. (13) is the same as that between the filter widths of L_{ij}^m and τ_{ij} in Eq. (3). Thus, $n/m = m/\ell$. This identity is necessary for the above expression to have the same model coefficients as in Eq. (3) and will also be useful when choosing the filter width ratios for the dynamic model. Analogous to Eq. (3), the quantities to be filtered for the evaluation of H_{ij} are constructed from the flowfield variables extracted at the filter level of the left-hand side term, which is $\widetilde{(\ )}$ here. Likewise, the tensors appearing in the second and third terms on the right-hand side are evaluated using the velocity field extracted at the $\widetilde{(\ )}$ level.

Equation Eq. (13) cannot be applied directly in an LES because the unfiltered flowfield denoted by u_i and ρ would be unavailable for the filtering operations needed to evaluate the terms in that equation. In order to make use of the above constitutive relationship to compute the model coefficients, we further assume that this relationship holds true after u_i is replaced with $\tilde{u}_i$, and ρ with $\bar{\rho}$. After these substitutions, we have

$$L_{ij}^m - \frac{\delta_{ij}}{3}L_{kk}^m = C_1 \frac{0.5L_{kk}^m}{\mathscr{L}_{kk}^m}\left(\mathscr{L}_{ij}^m - \frac{\delta_{ij}}{3}\mathscr{L}_{kk}^m\right) + C_2 \frac{0.5L_{kk}^m}{|\widehat{\widetilde{M}}|}\widehat{\widetilde{M}}_{ij} + C_3 \frac{0.5L_{kk}^m}{|\widehat{\widetilde{N}}|}\widehat{\widetilde{N}}_{ij}, \tag{17}$$

where

$$L_{ij}^m = \overline{\widehat{\rho}\tilde{u}_i\tilde{u}_j} - \frac{\overline{\widehat{\rho}\tilde{u}_i}\,\overline{\widehat{\rho}\tilde{u}_j}}{\overline{\widehat{\rho}}}, \quad \mathscr{L}_{ij}^m = \widetilde{\widehat{\rho}\hat{\tilde{u}}_i\hat{\tilde{u}}_j} - \frac{\widetilde{\widehat{\rho}\hat{\tilde{u}}_i}\,\widetilde{\widehat{\rho}\hat{\tilde{u}}_j}}{\widetilde{\widehat{\rho}}}, \quad \hat{\tilde{u}}_i = \frac{\overline{\widehat{\rho}\tilde{u}_i}}{\overline{\widehat{\rho}}}, \tag{18}$$

$$\widehat{\widetilde{M}}_{ij} = \widehat{\widetilde{S}}_{ik}\widehat{\widetilde{S}}_{kj} - \frac{\delta_{ij}}{3}\widehat{\widetilde{S}}_{kl}\widehat{\widetilde{S}}_{kl}, \quad \widehat{\widetilde{N}}_{ij} = \widehat{\widetilde{S}}_{ik}\widehat{\widetilde{\Omega}}_{kj} - \widehat{\widetilde{\Omega}}_{ik}\widehat{\widetilde{S}}_{kj}, \quad |\widehat{\widetilde{M}}| = \left(\widehat{\widetilde{M}}_{ij}\widehat{\widetilde{M}}_{ij}\right)^{1/2}, \quad |\widehat{\widetilde{N}}| = \left(\widehat{\widetilde{N}}_{ij}\widehat{\widetilde{N}}_{ij}\right)^{1/2}, \tag{19}$$

$$\widehat{\widetilde{S}}_{ij} = \frac{1}{2}\left(\frac{\partial \hat{\tilde{u}}_i}{\partial x_j} + \frac{\partial \hat{\tilde{u}}_j}{\partial x_i}\right), \quad \widehat{\widetilde{\Omega}}_{ij} = \frac{1}{2}\left(\frac{\partial \hat{\tilde{u}}_i}{\partial x_j} - \frac{\partial \hat{\tilde{u}}_j}{\partial x_i}\right). \tag{20}$$

Note that the "Germano identity" [29] has not been invoked anywhere during the derivation of the above equations, thus we avoid a formulation in which the model coefficients appear inside a filtering operation. The usual practice in models derived using the Germano identity has been to pull the model coefficient out of the test-filtering operation as if it were a constant, which is of course in direct contradiction with the spatially-varying nature of the model coefficient. Some ad hoc averaging or clipping procedures are then needed to maintain numerical stability in those models. The present model does not suffer from such an inconsistency. Using the test-filtered quantities at two separate levels, we can evaluate all of the terms appearing in Eq. (17), which are then used to solve for C_1, C_2, C_3.

Due to the L_{ij}^m tensor symmetry, Eq. (17) gives rise to a linear system of equations with six knowns and three unknowns. As there are fewer unknowns than knowns, a least-squares approach [30] can be used to minimize the error in the computed model coefficients. Let E_{ij} be the associated error of the overdetermined system, given by

$$E_{ij} = L_{ij}^d - C_1\mathscr{L}_{ij}^d - C_2\gamma_{ij} - C_3\lambda_{ij} \tag{21}$$

where

$$L_{ij}^d = L_{ij}^m - \frac{\delta_{ij}}{3}L_{kk}^m, \quad \mathscr{L}_{ij}^d = \frac{0.5L_{kk}^m}{\mathscr{L}_{kk}^m}\left(\mathscr{L}_{ij}^m - \frac{\delta_{ij}}{3}\mathscr{L}_{kk}^m\right), \quad \gamma_{ij} = \frac{0.5L_{kk}^m}{|\widehat{\widetilde{M}}|}\widehat{\widetilde{M}}_{ij}, \quad \lambda_{ij} = \frac{0.5L_{kk}^m}{|\widehat{\widetilde{N}}|}\widehat{\widetilde{N}}_{ij}. \tag{22}$$

The squared error is $Q = E_{ij}E_{ij} = \left(L_{ij}^d - C_1\mathscr{L}_{ij}^d - C_2\gamma_{ij} - C_3\lambda_{ij}\right)^2$. The optimum coefficients are determined by the constraint that minimizes the squared error [30], with

$$\frac{\partial Q}{\partial C_i} = 0 \quad (i = 1, 2, 3). \tag{23}$$

7

Application of the above criterion then leads to the following 3×3 linear system, the solution of which provides the dynamic model coefficients in a localized manner.

$$
\begin{bmatrix}
\mathscr{L}_{ij}^d \mathscr{L}_{ij}^d & \mathscr{L}_{ij}^d \gamma_{ij} & \mathscr{L}_{ij}^d \lambda_{ij} \\
\gamma_{ij} \mathscr{L}_{ij}^d & \gamma_{ij} \gamma_{ij} & \gamma_{ij} \lambda_{ij} \\
\lambda_{ij} \mathscr{L}_{ij}^d & \lambda_{ij} \gamma_{ij} & \lambda_{ij} \lambda_{ij}
\end{bmatrix}
\begin{bmatrix}
C_1 \\
C_2 \\
C_3
\end{bmatrix}
=
\begin{bmatrix}
L_{ij}^d \mathscr{L}_{ij}^d \\
L_{ij}^d \gamma_{ij} \\
L_{ij}^d \lambda_{ij}
\end{bmatrix}.
\tag{24}
$$

The SGS kinetic energy, k_{sgs}, needed in the model formulation, is obtained from the solution of a transport equation for k_{sgs} [31, 32], which is given by

$$
\frac{\partial \overline{\rho} k_{sgs}}{\partial t} + \frac{\partial \overline{\rho} \tilde{u}_i k_{sgs}}{\partial x_i} = -\tau_{ij} \widetilde{S}_{ij} + \frac{\partial}{\partial x_i} \left[\left(\tilde{\mu} + \frac{\mu_t}{\sigma_k} \right) \frac{\partial k_{sgs}}{\partial x_i} \right] - \overline{\rho} \varepsilon_{sgs}
\tag{25}
$$

where the three terms on the right-hand side represent the production, diffusion and dissipation of k_{sgs}, respectively, $\tilde{\mu}$ is the molecular viscosity, μ_t is the eddy viscosity and σ_k is the diffusivity parameter. The diffusion term includes the viscous diffusion and the model for the combined turbulent transport and pressure diffusion, based on the gradient-diffusion hypothesis which assumes that the joint turbulent transport and pressure diffusion of k_{sgs} is a diffusion process satisfying Fick's law. Since our nonlinear model given by Eq. (3) does not contain an eddy viscosity, we need to consider a separate linear eddy-viscosity model based on the Boussinesq closure to compute the μ_t needed in the above transport equation, as will be discussed.

Closure of the above transport equation for k_{sgs} requires a model for its dissipation rate, ε_{sgs}. The simplest available model is $\varepsilon_{sgs} = C_\varepsilon k_{sgs}^{3/2}/\overline{\Delta}$, which is derived from dimensional analysis. Although the model coefficient, C_ε, can be determined in a dynamic fashion using the information extracted from the resolved flowfield [33, 34, 35], our first attempt based on this simple model for ε_{sgs} did not yield satisfactory results. Hence, we solve a separate transport equation for ε_{sgs}, given by

$$
\frac{\partial \overline{\rho} \varepsilon_{sgs}}{\partial t} + \frac{\partial \overline{\rho} \tilde{u}_i \varepsilon_{sgs}}{\partial x_i} = -C_{\varepsilon_1} \tau_{ij} \widetilde{S}_{ij} \frac{\varepsilon_{sgs}}{k_{sgs}} + \frac{\partial}{\partial x_i} \left[\left(\tilde{\mu} + \frac{\mu_t}{\sigma_\varepsilon} \right) \frac{\partial \varepsilon_{sgs}}{\partial x_i} \right] - \overline{\rho} C_{\varepsilon_2} \frac{\varepsilon_{sgs}^2}{k_{sgs}}
\tag{26}
$$

where the three terms on the right-hand side represent the production, diffusion and destruction of ε_{sgs}, respectively, σ_ε is the diffusivity parameter, and C_{ε_1} and C_{ε_2} are the coefficients of the production and destruction terms, respectively. The diffusion term contains the viscous diffusion of ε_{sgs}, and the modeled transport terms are based on the gradient-diffusion hypothesis. These two transport equations are structurally identical to the $k - \varepsilon$ model equations commonly used in RANS [36], but the flow variables in the above equations naturally have a meaning different from the corresponding RANS variables in the $k - \varepsilon$ model equations. The production term in both transport equations is computed using τ_{ij} from Eq. (3). The viscous wall boundary conditions for k_{sgs} and ε_{sgs} are $k_{sgs} = 0$ and $\varepsilon_{sgs} = 0$. These two variables are not allowed to become negative as the transport equations are integrated in time, obviously due to the fact that a negative value of either variable would be unphysical.

A future task of this work will be to determine the coefficients of the production and destruction terms in the ε_{sgs} transport equation, which are C_{ε_1} and C_{ε_2}, respectively, using a dynamic procedure, such as the one outlined by Gallerano et al. [37]. In the present study, these two coefficients, as well as the two diffusivity parameters, σ_k and σ_ε, are set to constant values taken from the $k - \varepsilon$ model. For σ_k and σ_ε, we use 1 and 1.3, respectively, which are among the most common values used in the $k - \varepsilon$ model. For C_{ε_1} and C_{ε_2}, a more judicious choice must be made. Among various $k - \varepsilon$ model implementations, values ranging from 1.35 to 1.5 can be found for C_{ε_1}, and from 1.8 to 2 for C_{ε_2} [38]. As noted earlier, the flow solver used in this study requires a tenth-order compact filter [39], [40] to maintain numerical stability. This filter adds a certain

8

amount of numerical dissipation to the solution. One can compensate for that numerical dissipation by a proper selection of the physical dissipation parameters, which are controlled by C_{ε_1} and C_{ε_2}. We therefore set C_{ε_1} to 1.35, which is at the lower limit of its range, and C_{ε_2} to 2, which is at the upper limit of its range. A higher value of C_{ε_1} and/or a lower value of C_{ε_2} would lead to increased physical dissipation. We should also note that when constant values are used for C_{ε_1} and C_{ε_2}, these coefficients must be multiplied by a near-wall damping function to ensure proper behavior of the ε_{sgs} transport equation near the wall. Among various formulations that are available [38], we choose the following function which does not require a wall distance

$$f_d = \frac{\sqrt{Re_{sgs}^T}}{1 + \sqrt{Re_{sgs}^T}} \tag{27}$$

where Re_{sgs}^T is the SGS turbulence Reynolds number defined as $Re_{sgs}^T = \bar{\rho} k_{sgs}^2 / (\tilde{\mu} \varepsilon_{sgs})$.

An alternative to the transport equation for ε_{sgs} is the transport equation for the specific dissipation rate, $\omega_{sgs} = \varepsilon_{sgs}/(\beta^* k_{sgs})$, where β^* is a constant. In that case, the two transport equations solved for our nonlinear SGS model would become analogous to the $k - \omega$ RANS model equations [41]. The last term on the right-hand side of Eq. (25) would get replaced by $-\beta^* \bar{\rho} k_{sgs} \omega_{sgs}$ and ω_{sgs} would be obtained from the solution of a transport equation of identical structure to that of ε_{sgs}, as shown in Appendix A. In wall-bounded flows, the $k - \omega$ model is superior to the $k - \varepsilon$ model near the wall and does not require near-wall damping functions, but is known to be very sensitive to the freestream value of ω in free shear layers [42]. However, this weakness of the $k - \omega$ model is not an issue in the turbulent channel flow. Appendix A shows the application of our nonlinear model in combination with the two transport equations solved for k_{sgs} and ω_{sgs}, with the coefficients taken from the Wilcox-1988 $k - \omega$ model [43], to the turbulent channel flow problem with good success. However, the same strategy was found unsatisfactory for the speed bump flow, which is obviously much more complex as the flow encounters effects induced by strong pressure gradients and surface curvature as it moves over the bump, and also contains a free shear layer passing over a recirculating region. Thus, we revert back to the ε_{sgs} transport equation for the speed bump case.

The eddy viscosity appearing in the diffusion terms of the transport equations is obtained from a dynamic linear model, which has the following form

$$\tau_{ij} - \frac{2}{3}\bar{\rho} k_{sgs} \delta_{ij} = -2\bar{\rho} C_\mu \frac{k_{sgs}}{|\widetilde{S}|} \widetilde{S}_{ij}^d , \quad \widetilde{S}_{ij}^d = \widetilde{S}_{ij} - \frac{\delta_{ij}}{3}\widetilde{S}_{kk} , \quad |\widetilde{S}| = \left(2\widetilde{S}_{ij}\widetilde{S}_{ij}\right)^{1/2} , \tag{28}$$

where C_μ is the eddy-viscosity coefficient that is computed using a least-squares error approach as follows

$$C_\mu = -\frac{L_{ij}^d D_{ij}}{2D_{ij}D_{ij}} , \quad D_{ij} = \frac{0.5 L_{kk}^m}{|\widehat{\widetilde{S}}|} \widehat{\widetilde{S}}_{ij}^d , \quad \widehat{\widetilde{S}}_{ij}^d = \left(\widehat{\widetilde{S}}_{ij} - \frac{\delta_{ij}}{3}\widehat{\widetilde{S}}_{kk}\right) , \quad |\widehat{\widetilde{S}}| = \left(2\widehat{\widetilde{S}}_{ij}\widehat{\widetilde{S}}_{ij}\right)^{1/2} , \quad L_{ij}^d = L_{ij}^m - \frac{\delta_{ij}}{3}L_{kk}^m , \tag{29}$$

with L_{ij}^m given by Eq. (18), $\widetilde{S}_{ij}$ by Eq. (6), and $\widehat{\widetilde{S}}_{ij}$ by Eq. (20). This model can be considered as an alternative to the dynamic Smagorinsky model. It has been derived under the same assumptions given earlier, which are different from those employed in the Germano identity [29], using an alternative scaling that avoids the characteristic length scale in the formulation. The eddy viscosity in this model is $\mu_t = \bar{\rho} C_\mu k_{sgs} / \left(2\widetilde{S}_{ij}\widetilde{S}_{ij}\right)^{1/2}$, which is constrained to be positive as the concept of a negative eddy viscosity lacks rigorous justification. In contrast, the eddy viscosity of the Smagorinsky model is $\mu_t = \bar{\rho} C_S \overline{\Delta}^2 \left(2\widetilde{S}_{ij}\widetilde{S}_{ij}\right)^{1/2}$, where C_S is the Smagorinsky constant. The decision was made to not consider the dynamic Smagorinsky model [29, 44] in this study for two reasons: a) the model involves a characteristic length scale that comes with unresolved issues for anisotropic grids, as discussed earlier; b) the ill-founded practice regarding the treatment of the

9

model coefficient during the application of the Germano identity, described earlier, necessitates some ad hoc averaging or clipping procedures for model stabilization, which we prefer not to perform.

Another idea to determine the eddy viscosity needed in the diffusion terms of the two transport equations uses the following relation [45]

$$-\left(\tau_{ij} - \frac{2}{3}\overline{\rho}k_{sgs}\delta_{ij}\right)\widetilde{S}_{ij} = 2\mu_t^*\widetilde{S}_{ij}^d\widetilde{S}_{ij} \tag{30}$$

where τ_{ij} is taken from Eq. (3). This relation gives the equivalent eddy viscosity, μ_t^*, of a linear model that produces the same forward or backward energy scatter as that by the deviatoric component of our nonlinear model. This idea was not explored further in the present work but may be considered in the future.

As noted earlier, a least-squares approach is used to minimize the error in the coefficients of the dynamic nonlinear model. This means that there is a certain amount of error in the model coefficients, which creates the possibility of excessive k_{sgs} production at isolated instants during the simulation. This may, in turn, lead to numerical instability. To deal with this matter, a production limiter, derived from the realizability constraints of the modeled stresses, can be imposed. Mokhtarpoor and Heinz [46] showed that for a linear eddy-viscosity model, in order for the modeled stresses to satisfy the realizability constraints, the eddy-viscosity magnitude should be bounded as follows :

$$|\mu_t| \le \frac{23}{24\sqrt{3}}\frac{\overline{\rho}k_{sgs}}{|\widetilde{S}|^d} \tag{31}$$

where

$$|\widetilde{S}|^d = \left(2\widetilde{S}_{ij}^d\widetilde{S}_{ij}^d\right)^{1/2} , \quad \widetilde{S}_{ij}^d = \widetilde{S}_{ij} - \frac{\delta_{ij}}{3}\widetilde{S}_{kk} . \tag{32}$$

Based on the given eddy-viscosity limit, we can determine the maximum allowable production of k_{sgs} as

$$P_k^{max} = -\left(-2\mu_t^{max}\widetilde{S}_{ij}^d + \frac{2}{3}\overline{\rho}k_{sgs}\delta_{ij}\right)\widetilde{S}_{ij} = 2\mu_t^{max}(\widetilde{S}_{ij}^d \widetilde{S}_{ij}) - \frac{2}{3}\overline{\rho}k_{sgs}\widetilde{S}_{kk} \tag{33}$$

where

$$\mu_t^{max} = \frac{23}{24\sqrt{3}}\frac{\overline{\rho}k_{sgs}}{|\widetilde{S}|^d} . \tag{34}$$

As stated in the discussion of Eq. (30), the positive or negative production of k_{sgs} by the deviatoric component of our nonlinear model can be represented by a linear model with an equivalent eddy viscosity. Thus, the above positive production limiter derived for a linear model is also applicable to the present nonlinear model. This positive production limiter is enforced in both transport equations, since the $-\tau_{ij}\widetilde{S}_{ij}$ term appears on both right-hand sides. Hence, $-\tau_{ij}\widetilde{S}_{ij}$ is not allowed to exceed P_k^{max}. Furthermore, whenever the maximum allowable production value is reached, all SGS stress components are rescaled by the same factor so that the tensor product $-\tau_{ij}\widetilde{S}_{ij}$ becomes equal to the imposed limit. There is no limiter applied when negative production of k_{sgs} (or backscatter) occurs. Other than the positive production limiter procedure, no spatial/temporal averaging or clipping of the dynamic nonlinear model coefficients is employed.

To reiterate, the model requires test-filtering of the resolved flowfield at two levels. A test filter that can provide filter widths of at least several times the local grid size is necessary for this purpose. For LES based on finite-difference schemes, Shah [47] derived a suitable 3-point box filter that takes the nonuniform grid spacings into account. The coefficients of the filter were determined analytically by Shah [47] using Taylor series expansions and matching of the coefficients that appear on the two sides of the equation derived for the filtered quantity. On a uniform grid, the filter derived by Shah [47] can achieve a maximum filter width of only 2Δ, as it is a 3-point scheme. With a width of 2Δ on a uniform grid, Shah's filter becomes equivalent

to the box filter derived from the familiar Simpson's rule[††]. We follow the procedure of Shah [47] to derive a 7-point explicit central box filter and determine the coefficients of the filter numerically rather than analytically. The coefficients depend upon the specified ratio between the filter width and the grid spacing. This 7-point central filter accounts for nonuniform grid spacings, and allows test-filtering with a maximum width of 6Δ on a uniform grid. On nonuniform grids, the maximum filter width is not straightforward to define. However, for the grid considered in the present study, the grid stretching ratio in the wall-normal direction within the turbulence-containing region is rather mild, while the spanwise spacing is uniform, and the spacing variation along the streamwise direction is also gradual. We therefore assume that the maximum filter width that can be attained on the present nonuniform grid is also 6Δ. This assumption should hold as long as the grid spacing variations along the three directions of any given grid are relatively gradual. Proper one-sided and biased explicit formulations are derived for the grid points located near physical boundaries. In three dimensions, the filter is applied successively along the curvilinear grid lines. Filtering on physical boundaries is performed only along the two transverse directions.

We now discuss the choices of ℓ, m, n used in this study. Recall that the first parameter denotes the ratio of the grid filter width to the grid spacing, while the other two are the corresponding ratios of the two test-filtering operations. Our flow solver employs an optimized prefactored fourth-order accurate compact finite-difference scheme [26] to compute all spatial derivatives in the governing equations. This optimized scheme offers improved dispersion characteristics compared to the standard sixth- and eighth-order compact schemes [48]. It is derived from the standard eighth-order compact scheme that has been shown to possess spectral-like resolution [48]. The maximum resolvable wavenumber of this scheme based on a stringent error criterion for the dispersive characteristics of the scheme [26] was shown to be 1.85, which translates to $\ell = \pi/1.85 \approx 1.7$. The wavenumbers greater than this cutoff value would also be present in the resolved flowfield to some extent but the length scales corresponding to those wavenumbers would be poorly resolved and would additionally get damped by the tenth-order compact filtering scheme [39], [40] needed to maintain numerical stability. Hence, we will take the effective grid filter width for our discretization scheme as 1.7Δ. It was noted earlier that $n/m = m/\ell$ or $m^2 = n\ell$. Our 7-point test-filter would provide a maximum $n = 6$. With this maximum value, we get $m = \sqrt{(6 \cdot 1.7)} \approx 3.19$. This gives $n/m = m/\ell \approx 1.88$, which is only slightly less than 2[‡‡] and hence is a reasonable ratio that can be used in the dynamic model coefficient evaluation procedure. In the present study, the test-filtering operations are applied sequentially along the curvilinear grid lines. The corresponding test-filter coefficients are determined separately for each direction based on the specified m and n.

Finally, we should note that the SGS heat flux term also needs to be modeled in a compressible flow solver. Available models based on eddy diffusivity, scale-similarity or a linear combination of the two can be used for that purpose. In the present study, we employ an eddy diffusivity model based on the eddy viscosity of the linear model given by Eq. (28). To reiterate, the eddy viscosity is $\mu_t = \bar{\rho} C_\mu k_{sgs} / \left(2\widetilde{S}_{ij}\widetilde{S}_{ij}\right)^{1/2}$, where the dynamically determined C_μ is constrained to be positive. This eddy viscosity is used together with a turbulent Prandtl number of 0.9 to compute the SGS heat flux term. Implementation of the proposed modeling approach in the present study increases the computational cost per time step by a factor about two, relative to the cost of ILES, which employs no explicit SGS model. When compared to the DNS performed on 10.2 billion grid points with the same time step, the WRLES with the proposed model on the present grid, which contains about 659 million points, reduces the computational cost by a factor of about 8. Further reduction of the computational cost of the speed bump flow should be possible by coarsening of the vertical grid spacings in the region away from the wall.

During the course of this work, an alternative nonlinear model, which does not solve the transport equa-

---

[††]In one dimension, the corresponding test-filter is given by: $\widehat{f} = \frac{1}{6} f_{i-1} + \frac{2}{3} f_i + \frac{1}{6} f_{i+1}$, where i is the grid point index.

[‡‡]A filter width ratio close to 2 would ensure that the first test-filtering operation, performed at the $m\Delta$ level, extracts information from length scales that are reasonably well-resolved.

tions for k_{sgs} and its dissipation rate, but employs a simple model based on the scale-similarity assumption to model k_{sgs}, was also developed. This formulation produced very encouraging predictions over the windward side of the bump, but showed certain deficiencies over the leeward side. The main drawback of this simpler formulation is that it requires a backscatter limiter for numerical stability. The details of the alternative model formulation, and a summary of the results obtained with it are presented in Appendix B.

3 Computational Methodology

The code used in this study solves the unsteady three-dimensional compressible Navier-Stokes equations discretized on multiblock structured and overset grids. As noted earlier, an optimized prefactored fourth-order accurate compact finite-difference scheme [26] is used to compute all spatial derivatives in the governing equations. Third-order one-sided and biased schemes, respectively, are used on a boundary point and on the point next to the boundary. To maintain numerical stability, the present simulations use the tenth-order compact filtering scheme [39], [40], with matching one-sided biased formulations near the physical boundaries. A Beam-Warming type approximately factorized implicit scheme with subiterations is used for the time advancement [49]. More details of the simulation methodology can be found in the publications by Uzun and coworkers [50, 51, 52, 53, 11, 54, 55].

4 Test Case: Spanwise-Periodic Flow over the Speed Bump at Re_L = 2 Million

The speed-bump flow is the case chosen for the evaluation of the proposed nonlinear SGS model, along with the Vreman linear eddy-viscosity model and the no model ILES. Test runs were also performed using variations of the nonlinear model formulation given by Eq. (1), but those results are omitted because they were not more accurate than those obtained with the new nonlinear model. The spanwise-periodic configuration of the speed bump flow assumes a uniform two-dimensional profile along the span, which is described by $y(x) = h \exp\left(-(x/x_0)^2\right)$, where $x_0 = 0.195L$, x and y denote the axial and vertical directions, respectively (with z being the spanwise direction), $h = 0.085L$ is the bump height, and L is the width of the experimental model, that is taken as the reference length scale.

4.1 Simulation Details

The simulation parameters and the computational domain setup are identical to those previously used in the higher-fidelity simulation [5]. The Reynolds number based on the upstream reference velocity, U_∞, and L is Re_L = 2 million, while the freestream Mach number is 0.2. The corresponding Reynolds number based on h is 170000. The periodic domain span is set to $0.08L$. A schematic of the computational domain is shown in Figure 1. The inflow boundary of the domain is at $x/L = -0.8$ while the outflow boundary is at $x/L = 2$. The physical domain ends at $x/L = 1$. The region from $x/L = 1$ to 2 is the sponge zone, in which rapid grid stretching is applied along the streamwise direction. This zone contains a negligible number of points compared to the physical domain because of the significant grid stretching. The sponge zone dampens the turbulence in the flowfield before it reaches the outflow boundary, where standard characteristic outflow boundary conditions are applied. Viscous isothermal boundary conditions are imposed on the lower boundary, which contains the speed bump profile. The uniform wall temperature is set the same as the reference freestream value. The outer boundary in the vertical direction is placed at $y/L = 1$, on which a nonreflecting characteristic boundary condition is applied.

The computational grid for the present WRLES is extracted from that used in the DNS, the details of which can be found in Uzun and Malik [5]. This original grid is coarsened by a factor of four both along the streamwise and spanwise directions in much of the computational domain. A smaller streamwise coarsening factor is applied very near the inflow plane in order to allow the inflow boundary to properly inject the

turbulent fluctuations into the domain in conjunction with the inflow-generation technique (to be described below). The spanwise coarsening factor in that region is still equal to four. To enable a wall-resolved simulation, the grid resolution in the direction away from the wall is left unchanged. The coarsened grid contains about 659 million points. In this grid, the maximum Δs^+, which is the streamwise spacing in wall units, in the attached region upstream of separation is about 32 to 36 units, while the maximum Δz^+, which is the spanwise spacing in wall units, is 16 to 24 units in the same region. The separated region is covered by about 500 points in the streamwise direction. There are 432 uniform points along the span of $0.08L$. The largest values of Δs^+ and Δz^+ in the recovery region are 48 and 14 units, respectively, and are found near the end of the physical domain. The wall-normal grid spacing, Δn^+, adjacent to the wall varies from 0.5 to 1 in the attached region. The wall-normal spacing increases with distance from the wall. In the region upstream of the bump, the largest Δn^+ found in the vicinity of the attached boundary-layer edge is around 5–7 wall units; in the acceleration region, the maximum value is about 14 units. In the downstream recovery region, the largest Δn^+ values around the boundary-layer edge are found near the end of the physical domain, and have a value of about 50. There are about 200 points from the wall to the outer edge of the free shear layer at the beginning of flow separation. The line through the thickest section of the separation bubble is discretized using about 300 points across the bubble in the vertical direction. Further details of the original grid from which the current grid has been extracted can be found in Uzun and Malik [5].
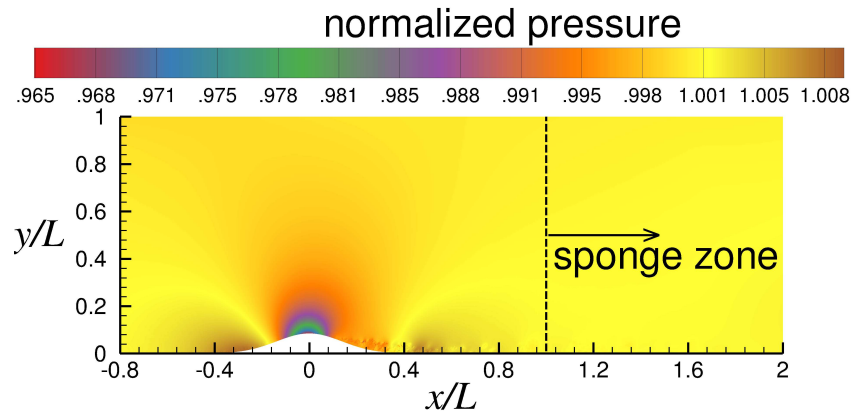

Figure 1. Computational domain schematic. Contours denote the instantaneous pressure normalized by the reference value.

The second-order accurate implicit Beam-Warming scheme [49] is used for the time integration. The time step taken in the WRLES is the same as that previously used in the DNS [5]. It takes 178955 time steps to compute a time interval of L/U_∞. For the turbulent inflow generation, we use the same procedure as in the DNS [5], which is based on the rescaling-recycling technique discussed in Uzun and Malik [54], [56]. The present technique only recycles the turbulent fluctuations while keeping the mean inflow profile fixed. The mean flow imposed at the inflow boundary is taken from a RANS calculation performed with the low-Reynolds-number correction version of the Spalart-Allmaras model [57]. The mean inflow boundary-layer thickness at $x/L = -0.8$ is $\delta_{in} \approx 0.0055L$, giving $\delta/h \approx 0.065$. The corresponding inflow momentum-thickness Reynolds number is $Re_\theta \approx 1035$. The same mean inflow profile was also used in the DNS [5]. The distance between the inflow and recycle planes is about $12\delta_{in}$.

Results from three WRLES calculations will be shown and discussed in the next subsection. As noted earlier, the first WRLES is performed as an ILES, with no explicit SGS model, while the second WRLES is performed with the Vreman model, using a constant model coefficient of $0.025^{§§}$. The third WRLES is

---

§§This value is chosen based on past experience with this model in other problems. Note that the "standard" value of 0.07 found by Vreman [10] is for homogeneous isotropic turbulence, which is not the case for the present problem.

performed using the new dynamic nonlinear SGS model. The ILES treats the numerical dissipation in the tenth-order compact filter [39], [40], needed to maintain numerical stability, as an implicit SGS model. This filter is also active when an explicit SGS model is used in the other two WRLES, because using an explicit SGS model alone does not provide sufficient numerical stability that completely eliminates the spurious oscillations generated by the application of the nondissipative discretization scheme to the conservative form of the governing equations. The statistical results were time averaged over $4.8L/U_\infty$ for the ILES, $4L/U_\infty$ for the WRLES with the Vreman model, and $4.6L/U_\infty$ for the WRLES with the dynamic nonlinear model. The DNS results that will be used in the comparisons were gathered over $11L/U_\infty$. Although the WRLES results were not time-averaged as long as the DNS, the smaller statistical samples still provide sufficient information about the overall flow behavior under different modeling approaches. Hence, taking a longer average in these calculations would not significantly change the findings.

4.2 Results

We now examine the results from the three WRLES and compare with the earlier DNS [5]. Figure 2 provides the surface pressure coefficient, C_p, and the skin-friction coefficient, C_f, distributions. These coefficients are given by

$$C_p = \frac{\langle p \rangle - p_\infty}{\frac{1}{2}\rho_\infty U_\infty^2} \quad \text{and} \quad C_f = \frac{\langle \tau_w \rangle}{\frac{1}{2}\rho_\infty U_\infty^2} \,, \tag{35}$$

where ρ_∞, p_∞, U_∞, respectively, are the reference freestream density, pressure and velocity, $\langle p \rangle$ is the mean surface pressure and $\langle \tau_w \rangle$ is the mean wall shear stress. The C_p distribution is compared with the data taken on the centerline of the experiment by Williams et al. [7] at $Re_L \approx 1.98$ million. The C_f distribution is compared with the measurements available from a separate experiment conducted by Gray et al. [9] at $Re_L = 2$ million. Before examining the WRLES results, we first note that the DNS result shows very good agreement with the experimental C_f measurement along the bump centerline over the entire attached region. Some C_f differences are found in the separation and recovery regions, which are not totally surprising. The three-dimensional effects of the experimental configuration, which are not duplicated in the present spanwise-periodic simulations, are expected to have more of an impact in the separation and recovery regions of the flow. The C_p distribution of the DNS also shows reasonable overall agreement with the experimental data from Williams et al. [7]. The plateau observed in the C_p distribution downstream of the apex is caused by the flow separation. The pressure rise observed after the plateau appears slightly delayed in the simulation relative to the experiment, which suggests that the reattachment location in the simulation is delayed relative to the experiment. This difference is not a surprise given that no attempt was made to model the three-dimensional configuration of the experiment.

Examining the WRLES results, we observe that the SGS modeling approach has a significant impact on the separated flow region. The C_f plot shows that the ILES generates a much weaker reversed flow region relative to the DNS. Employing the Vreman SGS model makes the prediction even further removed from the DNS result; the separated region has nearly disappeared in that case. The corresponding C_p distributions reflect these differences in the separation region. Another interesting observation is that, for the ILES, the C_p peak is strengthened while the C_f peak is weakened. The WRLES with the Vreman SGS model lowers the C_f peak further while slightly increasing the C_p peak relative to the ILES. These higher C_p peaks are believed to be due to the different effective body shapes originating from the weak or nonexistent separation in those two cases. All in all, such predictions of these two WRLES are clearly unsatisfactory. We find that the WRLES with the new dynamic nonlinear model provides much improved predictions relative to the other two modeling approaches. The overall C_f agreement of this case with the DNS data is quite satisfactory, but there are some noticeable differences. In the far upstream region, the C_f prediction with the nonlinear model is found to be slightly higher relative to the DNS, and slightly lower in the early part of the acceleration region. The peak C_f is also slightly lower than the corresponding DNS value. The separation

14

point in the WRLES with the nonlinear model is at $x/L \approx 0.091$, and at about $x/L = 0.1$ in the DNS. The C_f magnitudes within the separation region suggest a stronger reversed flow in the WRLES relative to the DNS, which will be analyzed in more detail shortly. The recovery zone C_f values in the WRLES are slightly higher. This could be partly due to the shorter statistical sample of the WRLES. The recovery zone contains large-scale structures generated within the separated shear layer, which normally require a long time average for full statistical convergence. The C_p distribution of the WRLES with the nonlinear model shows that the C_p plateau within the separation region is higher relative to that of the DNS. This is again a consequence of the stronger reversed flow. The earlier separation in the WRLES affects the effective body shape felt by the upstream flow and this leads to a slight reduction of the peak C_p in the WRLES. For brevity, the remaining analysis will mostly focus on the WRLES results obtained with the dynamic nonlinear model and the comparisons with the DNS. We will also show some additional results from the ILES and the WRLES with the Vreman model at critical locations of the flowfield.
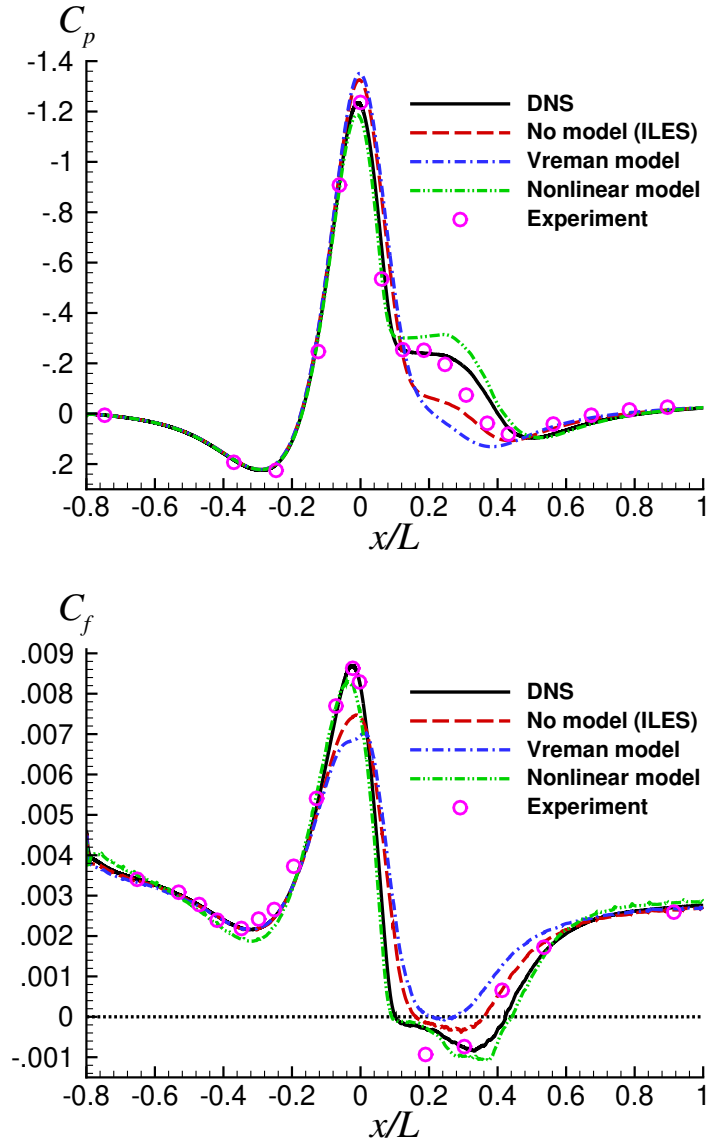
Figure 2. Effect of the SGS model on C_p and C_f distributions.

(a) $x/L = -0.5$

(b) $x/L = -0.4$

(c) $x/L = -0.3$

(d) $x/L = -0.2$

(e) $x/L = -0.1$

(f) $x/L = 0$
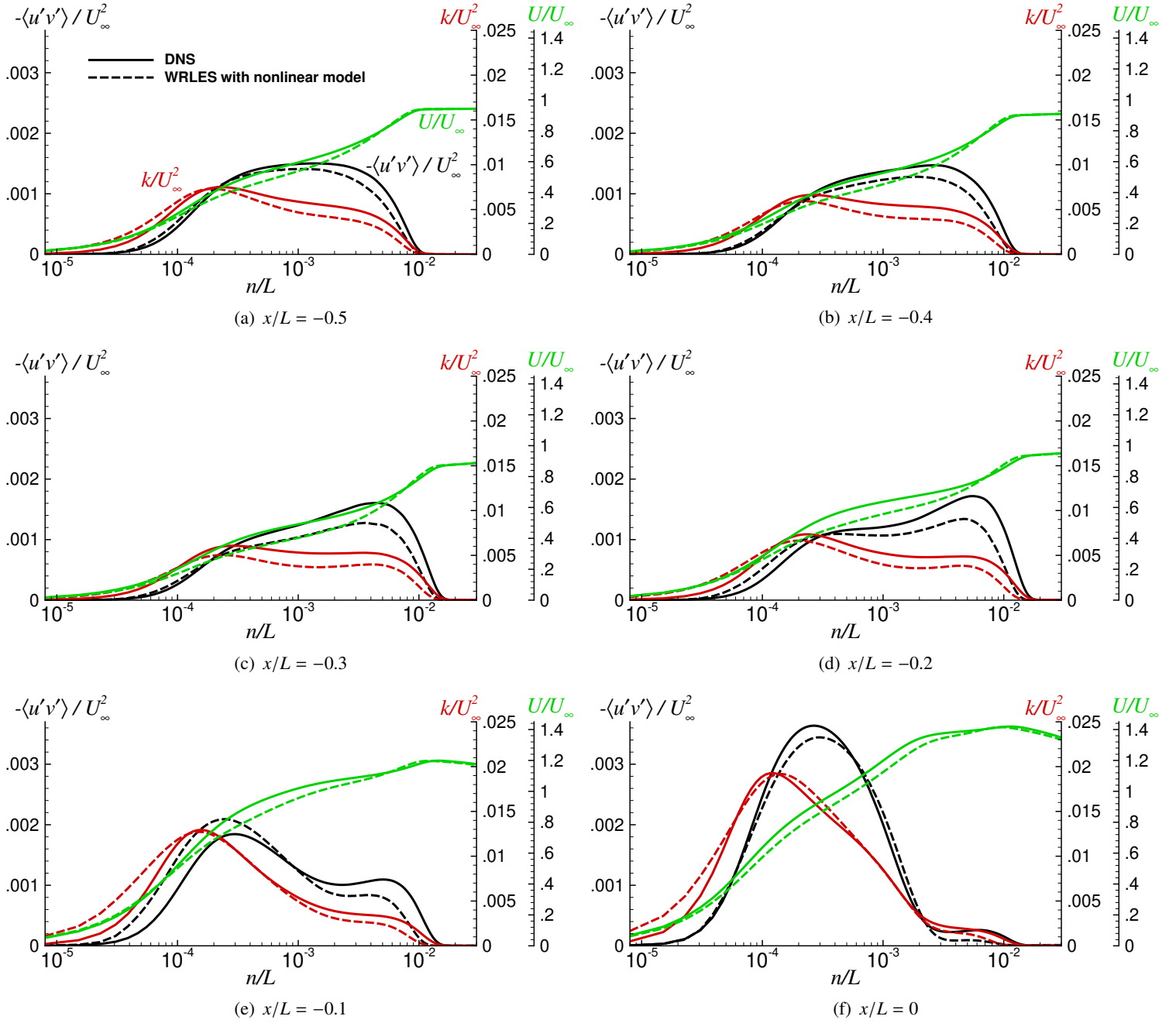
Figure 3. Wall-normal profiles in the region where $-0.5 \leq x/L \leq 0$.

We now consider the evolution of mean streamwise velocity, U/U_∞, Reynolds shear stress, $-\langle u'v' \rangle/U_\infty^2$, and turbulent kinetic energy (TKE), $k/U_\infty^2 = (\langle u'u' \rangle + \langle v'v' \rangle + \langle w'w' \rangle)/2U_\infty^2$ profiles in the region from $x/L = -0.5$ to $x/L = 1$. Here, $\langle u'u' \rangle$, $\langle v'v' \rangle$, and $\langle w'w' \rangle$, respectively, are the streamwise, wall-normal and spanwise components of Reynolds stress in the local orthogonal system at a given station, and the $\langle \ \rangle$ operator denotes averaging in time and along the span. The Reynolds shear stress and the mean streamwise velocity are also defined with respect to the local orthogonal system. The profiles are normalized using the reference freestream velocity, U_∞. The wall-normal distance from the bump surface, n, is normalized by L and is plotted in logarithmic scale. To enable a meaningful comparison with the fully resolved quantities from

16

the DNS, all Reynolds stresses and TKE are computed by adding up the resolved and modeled components in the WRLES. The region of comparison is divided into three separate subregions, $-0.5 \leq x/L \leq 0$, $0.05 \leq x/L \leq 0.4$, and $0.5 \leq x/L \leq 1$, as depicted in Figures 3, 4 and 5, respectively. To allow easier tracking of the profile evolutions in these subregions, the subfigures of each figure use the same range for the vertical axis for a given quantity.
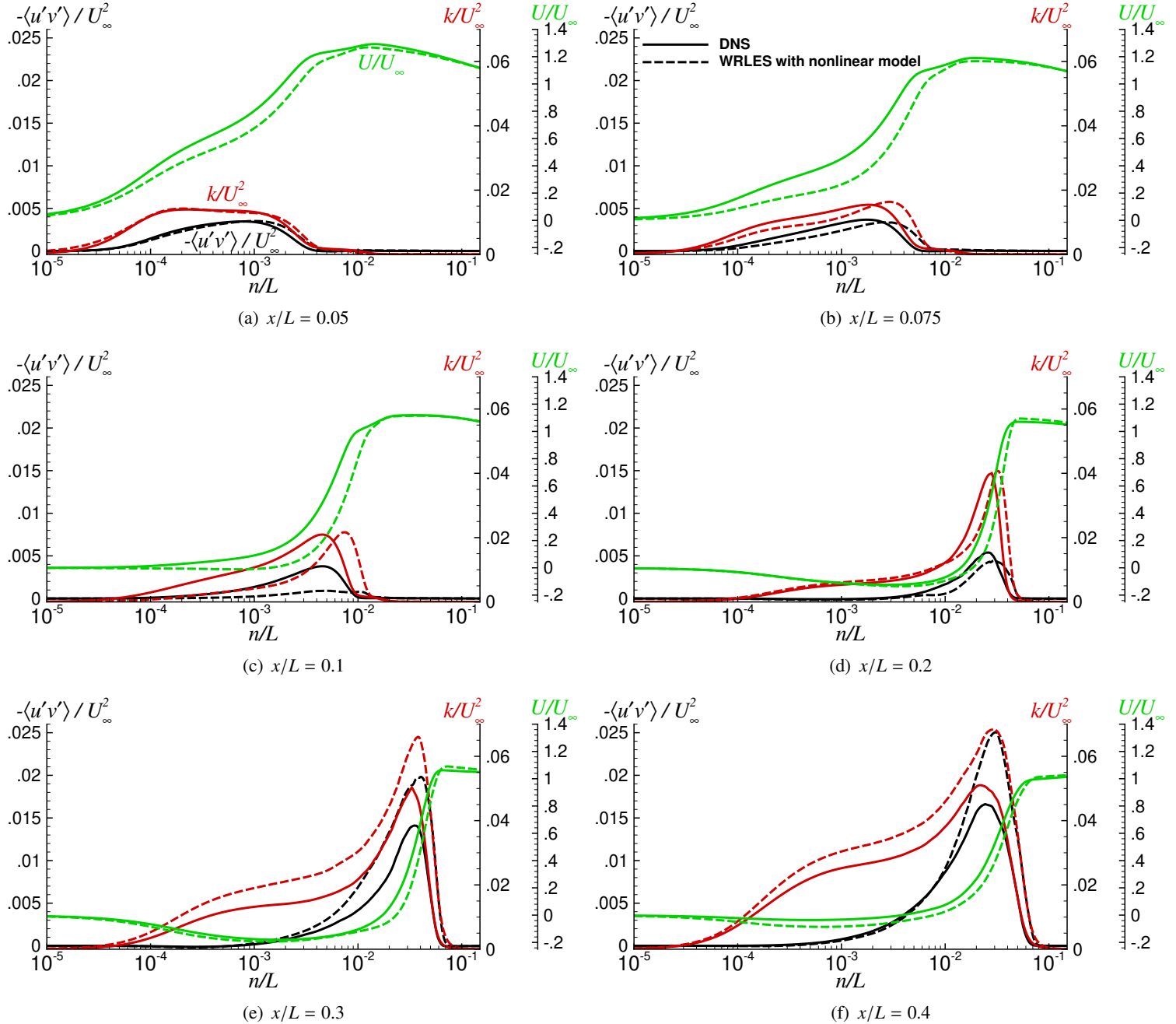

Figure 4. **Wall-normal profiles in the region where $0.05 \leq x/L \leq 0.4$.**

The profiles on the windward side of the bump, depicted in Figure 3, show that the response of the mean streamwise velocity profile to the adverse and favorable pressure gradients encountered in that region is

17

captured to some extent by the WRLES, when compared to the DNS, but better quantitative agreement with the DNS is desirable. The skin-friction differences in the incoming flow, as noted earlier, are associated with the mean velocity profile differences seen at the first few stations depicted in Figure 3. These velocity profile differences, which are mainly found in the logarithmic layer, convect downstream as the incoming flow nears the bump and begins to accelerate. As seen in the C_p plot, the incoming boundary layer encounters an adverse pressure gradient that is initially mild but becomes progressively stronger as the flow approaches the bump foot at $x/L \approx -0.29$. This decreases the maximum streamwise velocity over that region. The pressure gradient becomes strongly favorable starting at $x/L \approx -0.29$ until very near the bump apex. The acceleration causes a significant increase in the maximum velocity, which exceeds $1.4U_\infty$ at the apex. The associated changes in the Reynolds shear stress and TKE profiles over the windward side of the bump, as observed in the DNS, are also captured qualitatively in the WRLES but better quantitative agreement with the DNS is once again desirable. As discussed in Uzun and Malik [5], an internal layer develops within the accelerated flow, which is believed to be triggered by the switch from the mild adverse to strong favorable pressure gradient at the foot of the bump. Strong peaks in all Reynolds stress components emerge as this internal layer continues its development within the favorable pressure gradient region. The original peak of the Reynolds shear stress is located away from the wall; the emergence of a strong inner peak closer to the wall is an indication of the emerging internal layer. The outer Reynolds shear stress peak decays due to the interaction with the favorable pressure gradient and also with the convex streamline curvature found in the late stages of acceleration near the apex. Meanwhile, the original peak of the TKE profile in the upstream boundary layer is positioned close to the wall; hence, the TKE peak becomes engulfed within the developing internal layer and is further strengthened. The emerging near-wall Reynolds shear stress peak seems a bit more energetic at $x/L = -0.1$ in the WRLES but this does not appear to be much of a detriment to the reasonable agreement found with the DNS at the apex, where the TKE peak agreement is also acceptable.

We observe in Figure 3 that, in the WRLES, the TKE tends to be generally overpredicted in the near-wall region and underpredicted in the outer region, except at the apex, where only the near-wall overprediction remains. The Reynolds shear stress profiles also show similar overprediction near the wall and underprediction in the outer region at some stations. This shortcoming suggests insufficient ε_{sgs} in the near-wall region, and excessive ε_{sgs} in the outer region of the boundary layer over much of the windward side of the bump. This is also the likely reason for the deficit found in the mean velocity profile logarithmic layer noted earlier and the associated differences in the skin-friction distribution relative to the DNS result. We believe these related issues to be a consequence of setting empirical constants for the production and destruction terms of the ε_{sgs} transport equation, in combination with a near-wall damping function. This observation thus provides the motivation for the dynamic evaluation of the production and destruction term coefficients in the ε_{sgs} transport equation, as stated earlier, and remains a future task of this work.

Although not shown here, the mean flow and Reynolds stress predictions of the ILES and the WRLES with the Vreman model were found acceptable on the windward side of the bump until $x/L \approx -0.2$, as hinted by the reasonable C_f predictions of those two cases over that region. However, as we will show later, significant differences relative to the WRLES with the nonlinear model and the DNS appear once the flow enters the late stage of acceleration in those two cases.

Examination of the profiles in the deceleration and separation region, depicted in Figure 4, shows generally reasonable similarity between the DNS and the WRLES but there are some notable differences. The mean velocity profile response to the adverse pressure gradient immediately past the apex over the leeward side of the bump, as shown by the profiles at $x/L = 0.05$, 0.075, and 0.1, is slightly faster in the WRLES relative to the DNS. We believe this difference is due to the mean velocity profile difference at entrance of the adverse pressure gradient region, as seen in the apex profiles depicted in Figure 3(f), which displays a lower intercept of the logarithmic layer for the WRLES. The adverse pressure gradient decelerates both the near-wall and outer regions of the boundary layer, and this leads to the formation of an intermediate buffer zone that looks much like a free shear layer. Once all near-wall momentum has vanished, the flow separation

occurs at $x/L \approx 0.091$ in the WRLES, and at about $x/L = 0.1$ in the DNS. The TKE peak at the apex, which is positioned very close to the wall within the internal layer, begins to weaken in both cases as the flow decelerates toward separation. However, this process happens slightly faster in the WRLES. The weakening of the TKE peak is due to the reduction in the near-wall velocity shear by the adverse pressure gradient. This reduces the production of the streamwise stress, which is the largest contributor to the TKE. Meanwhile, the original peak in the Reynolds shear stress profile, initially positioned further from the wall relative to the TKE peak, shifts outward while maintaining strength in the deceleration region from $x/L = 0$ to 0.1 in the DNS, but displays considerable weakening in the WRLES during the same phase. The reason for this somewhat peculiar behavior is not well understood at the moment, but it is likely related to differences found between the two cases at the entrance of the adverse pressure gradient region, as noted earlier. We also see the development of an outer TKE peak near the Reynolds shear stress peak, as the flow decelerates. The profiles at $x/L = 0.1$ show that the new TKE peak and the Reynolds shear stress peak are located quite closely within the free shear layer in both cases. The location of this peak is a bit further away from the wall in the WRLES. As discussed in Uzun and Malik [5], these findings suggest a close connection between the internal layer that develops upstream within the acceleration region, and the free shear layer that emerges in the deceleration region.

Such differences in the deceleration region between the two cases alter the "initial conditions" of the separated flow, hence affecting what happens within the separation zone. Although the profile comparisons at $x/L = 0.2$ show similar TKE and Reynolds shear stress peak strengths between the two cases, the WRLES generates relatively stronger TKE and Reynolds shear stress peaks by the time the free shear layer reaches $x/L = 0.3$, which is located roughly in the middle of the separation region. Similar stronger peaks within the shear layer are again found in the WRLES at $x/L = 0.4$, which is positioned in the late stage of separation. The mean velocity profiles, shown at the stations from $x/L = 0.2$ to 0.4, are fairly similar between the two cases. The stronger reversed flow in the WRLES is indicated by the higher velocity magnitudes found in between the wall and the free shear layer. As discussed in Uzun and Malik [5], the separated shear layer generates energetic eddies, as evidenced by the high TKE levels within the shear layer, that impinge on the wall in the vicinity of the reattachment point. Some of these eddies get diverted into the reversed flow region and move upstream along the wall, while the rest get dragged downstream by the recovery flow. Consequently, high levels of streamwise and spanwise Reynolds stresses, which lead to increased TKE levels, are found near the reattachment point within the recirculating flow. The peak TKE levels within the free shear layer are therefore correlated with the sizable TKE levels observed in the recirculating flow. These levels drop as the distance from the reattachment point increases within the reversed flow region because the near-wall eddies slow down as they move further upstream. It was also seen in Uzun and Malik [5] that although there is a small rise in the wall-normal and shear stress components in the reversed flow region near the wall, those increases are not as significant, since the wall-normal velocity fluctuations are rather small in that part of the flow. Thus, the rise of the Reynolds shear stress within the recirculating region is not as strong as that of the TKE. These trends are duplicated in the WRLES, which shows considerably higher TKE levels in the recirculating flow region between the free shear layer and the wall at $x/L = 0.3$, relative to the DNS. This is another indication of the stronger reversed flow in the WRLES.

Figure 6(a) shows the mean velocity and the total Reynolds shear stress profiles from the three WRLES cases at the bump apex where $x/L = 0$, and the comparison against the DNS data. The mean velocity profile shapes for the ILES and Vreman model cases reveal the deviations from the DNS results. Their Reynolds shear stress peaks are relatively weaker. The profiles obtained with the nonlinear model are in better agreement with the DNS results. Hence, we see that the new dynamic nonlinear model leads to a more satisfactory prediction of the flow development in the late stages of flow acceleration on the windward side of the bump. Figure 6(b) shows the mean velocity and the total Reynolds shear stress profiles from the ILES and the WRLES with the Vreman model at $x/L = 0.25$, which is located in the middle of the separation region, and the comparison against the other data. As seen earlier, the ILES predicts much weaker separation

while the WRLES with the Vreman model shows almost no separation. The mean velocity profile shapes from those two cases reflect those discrepancies. Their corresponding Reynolds shear stress profiles are also far from the DNS result. Once again, the mean velocity profile obtained with the nonlinear model is much closer to the DNS result. While the total Reynolds shear stress profile obtained with the nonlinear model is not perfect, it shows the best overall qualitative agreement with the DNS. The shear stress peak among the three WRLES results is the highest with the nonlinear model as it leads to the strongest flow separation.
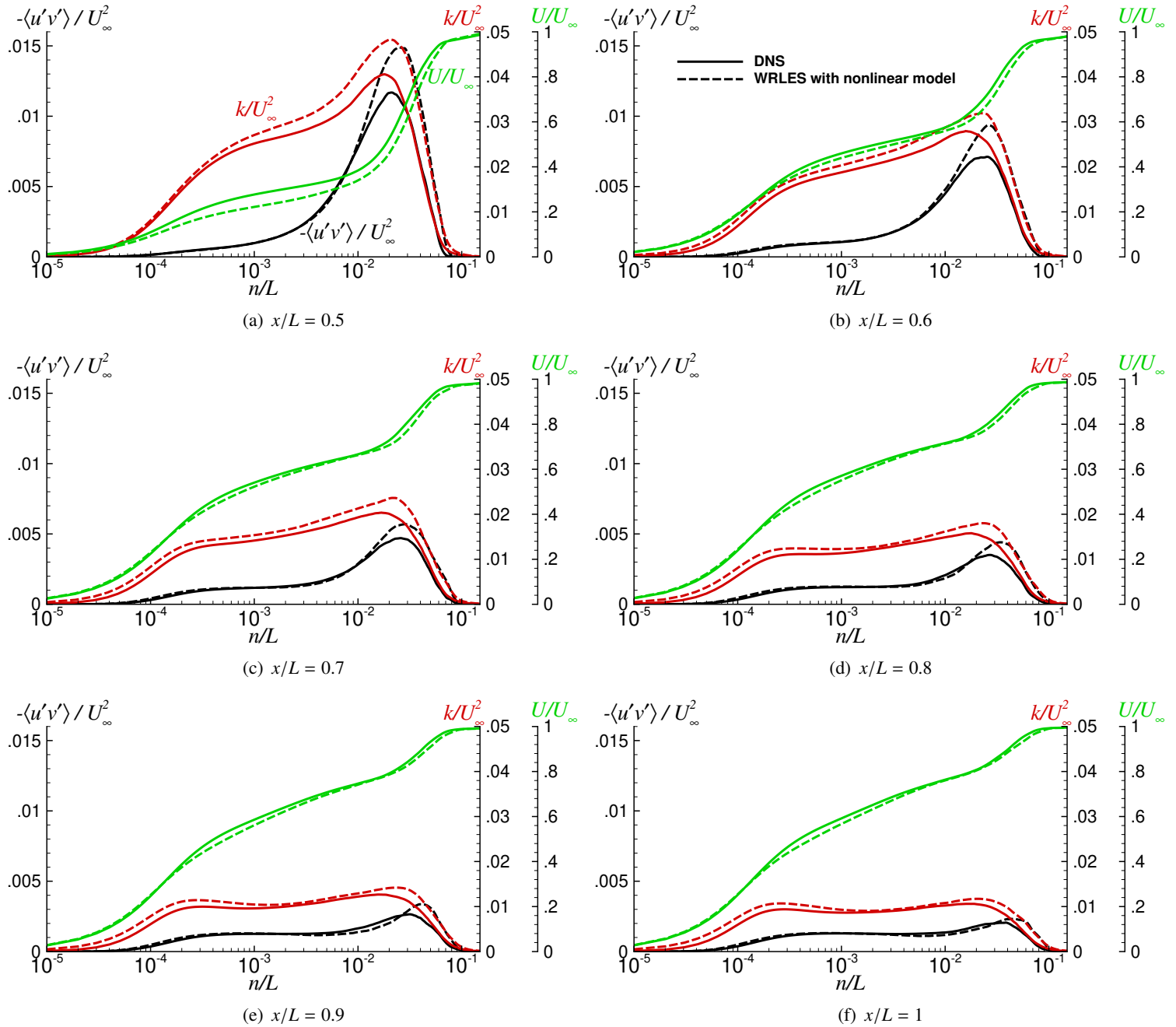
Figure 5. Wall-normal profiles in the region where $0.5 \leq x/L \leq 1$.
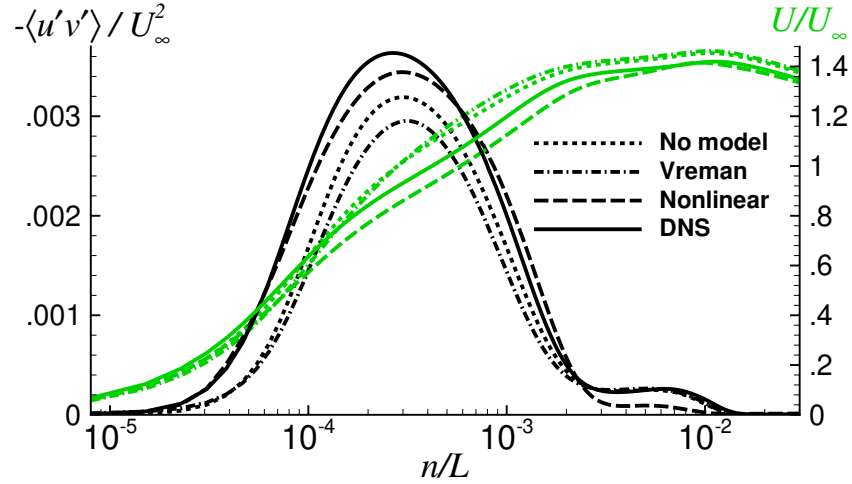
(a) $x/L = 0$
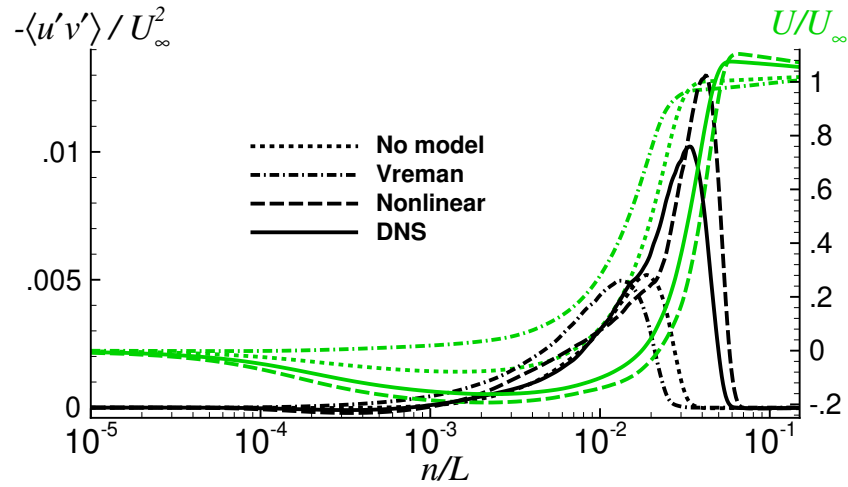
(b) $x/L = 0.25$

Figure 6. Comparison of the mean velocity and total Reynolds shear stress profiles.

The flow reattachment is at $x/L \approx 0.423$ and 0.441 in the DNS and the WRLES with the nonlinear model, respectively. The profiles taken within the recovery zone following separation, depicted in Figure 5, show reasonable overall similarity between the two simulations. The initially high near-wall TKE levels, found in the vicinity of the reattachment point, drop as the energetic eddies from the impinging shear layer get dragged along the wall beneath the recovery flow and get weakened. The weakly favorable pressure gradient of the recovery region causes the free shear layer to gradually dissipate as the flow moves downstream, as indicated by the corresponding shape changes in the mean velocity profiles. This causes the TKE and Reynolds shear stress peaks within the shear layer to weaken with the streamwise distance. Those outer peaks would eventually disappear with a sufficiently long domain size. At the same time, another internal layer begins to emerge near the wall within the recovery flow, as indicated by the formation of a new TKE peak there. The Reynolds shear stress profile also appears to be developing a new peak close to the wall but the computational domain size is not sufficiently long for that process to complete. As the recovery flow evolves, the WRLES shows relatively higher TKE levels near the wall, similar to what was observed previously over the windward side of the bump.
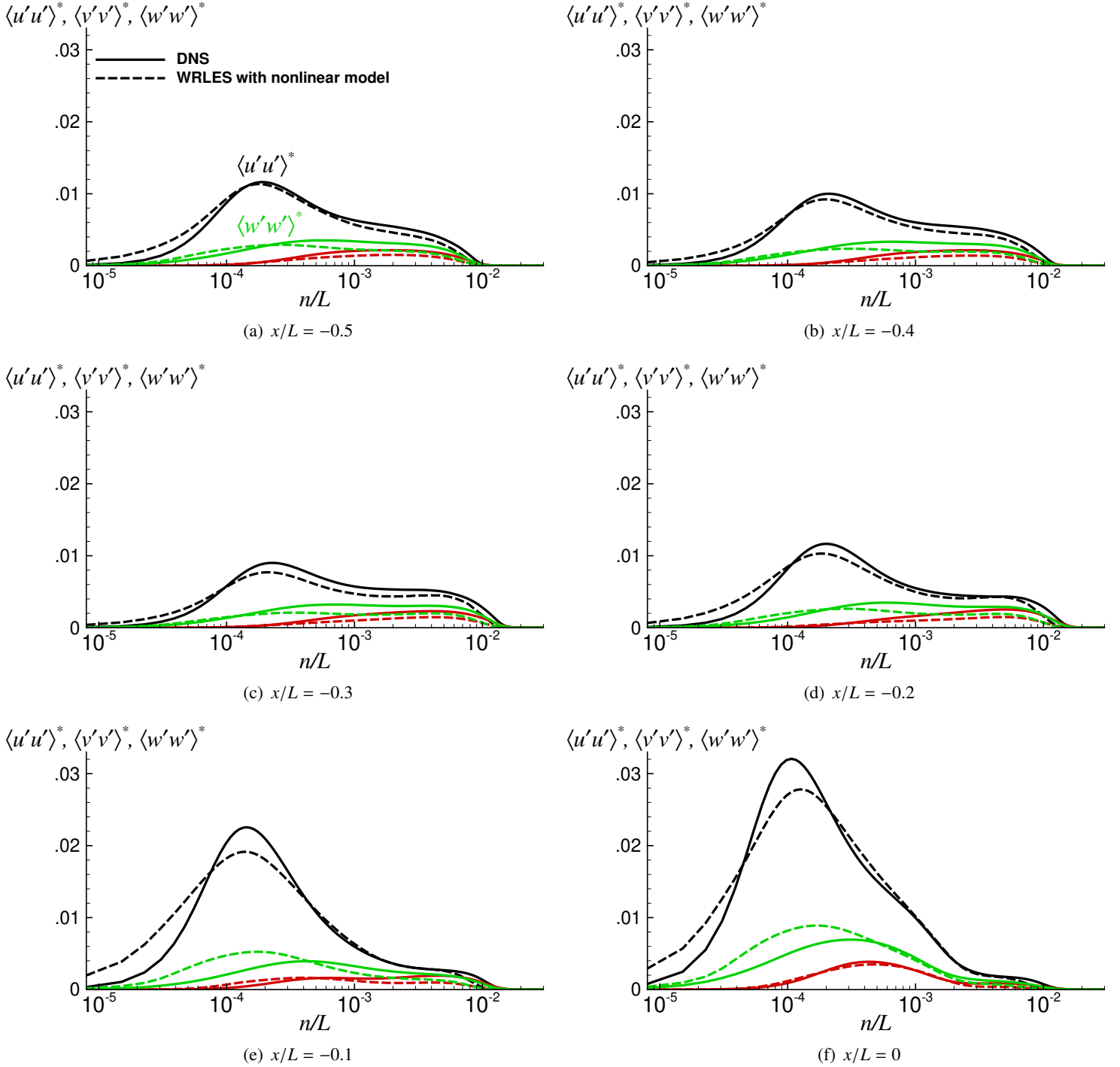
Figure 7. Normal Reynolds stress profiles in the region where $-0.5 \leq x/L \leq 0$.

Next, we examine the evolution of the normal Reynolds stress components, defined in the local orthogonal system at various stations. Figures 7, 8 and 9 plot the normalized $\langle u'u'\rangle^* = \langle u'u'\rangle/U_\infty^2$, $\langle v'v'\rangle^* = \langle v'v'\rangle/U_\infty^2$, and $\langle w'w'\rangle^* = \langle w'w'\rangle/U_\infty^2$ profile comparisons between the two simulations, in the three subregions used for the previous analysis. For the WRLES, they are presented as the sum of the resolved and modeled components. The profiles taken over the windward side of the bump, depicted in Figure 7, show

qualitative agreement with the DNS. The overprediction of the TKE in the near-wall region and its under-prediction in the outer region translate into the normal Reynolds stress profile differences as seen here. As noted earlier, the pressure gradient becomes strongly favorable at $x/L \approx -0.29$ until very near the bump apex, which leads to strong flow acceleration and generation of an internal layer near the wall. Thus, we see a peak amplitude growth and other associated changes in the profiles downstream of $x/L = 0.3$ in Figure 7. As the flow nears the apex, the peak amplitude of $\langle w'w' \rangle^*$ is found to be stronger in the WRLES relative to that in the DNS, while the peak amplitude of $\langle u'u' \rangle^*$ is relatively lower, and that of $\langle v'v' \rangle^*$ is about the same. Despite such differences, the mean streamwise velocity and the Reynolds shear stress profiles in the late stages of acceleration displayed a favorable agreement in our earlier analysis.

The profiles in the deceleration and separation region, shown in Figure 8, reflect the similarities and differences noted earlier between the two cases in that region. To reiterate, the slightly faster flow response to the adverse pressure gradient affects the mean velocity profile shapes in the deceleration region of the WRLES. This, in turn, impacts the Reynolds stress distributions, as seen at the first three stations of Figure 8, and leads to initial condition differences of the separated flow between the two cases. The separation region shows reasonable overall similarity between the two cases. The peak normal stress amplitudes, located within the free shear layer, are higher in the WRLES in the middle and late stages of separation. The stronger recirculating flow in the WRLES is again shown by the relatively higher normal and spanwise stress components near the wall at $x/L = 0.3$. Reasonable overall agreement between the two cases is maintained once the separated flow reattaches and the recovery begins, as seen in Figure 9. The higher near-wall TKE in that region observed in the WRLES is due to the higher streamwise Reynolds stress near the wall.

In conclusion, the comparisons with the DNS data show promising success for the new dynamic non-linear SGS model. Although better agreement with the DNS data remains desirable in certain parts of the flowfield, the main features of the problem have been predicted much better than we have been able to achieve with any other SGS model on the given grid. It is hoped that the dynamic evaluation of the production and destruction term coefficients in the ε_{sgs} transport equation, or more advanced dissipation models that can be used in the closure of the k_{sgs} transport equation without the need to solve a separate transport equation for ε_{sgs}, will be able to rectify the identified shortcomings of the model.

5   Summary and Concluding Remarks

A new dynamic nonlinear subgrid-scale model, inspired by the triple model idea of Bardina et al. [13] that was proposed nearly four decades ago, has been developed for large-eddy simulations, which is expected to be applicable to a wide variety of complex turbulent flows involving pressure gradients, surface curvature and separation. The present model replaces the scale-similarity term of the original triple model, which is not Galilean invariant, with the modified Leonard stress tensor, which is Galilean invariant. The model also contains two nonlinear terms containing the products of the strain-rate and rotation-rate tensors. The first nonlinear term, which is capable of generating both dissipation and backscatter depending on the sign of its coefficient, replaces the linear eddy-viscosity term of the original triple model. The second nonlinear term, which is the same as the nonlinear term of the original triple model, does not generate dissipation or backscatter, but accounts for anisotropy. The model derivation is based on the assumption that the constitutive relation for the subgrid-scale stresses is also applicable to length scales several times the size of the largest subgrid scales. The specific formulation of the model does not use a characteristic length scale for any of its terms and hence naturally avoids the ambiguities associated with defining a proper length scale for anisotropic grids. The model additionally requires the solution of two transport equations, one for the subgrid kinetic energy, and another one for its dissipation rate. Test-filtering of the resolved flowfield at two separate levels is performed for the dynamic determination of the three model coefficients with a localized procedure. Other than the use of a production limiter to prevent excessive subgrid kinetic energy generation,

which is derived from the realizability constraints of the modeled stresses, no spatial/temporal averaging of any kind or any other clipping is applied to the model coefficients.
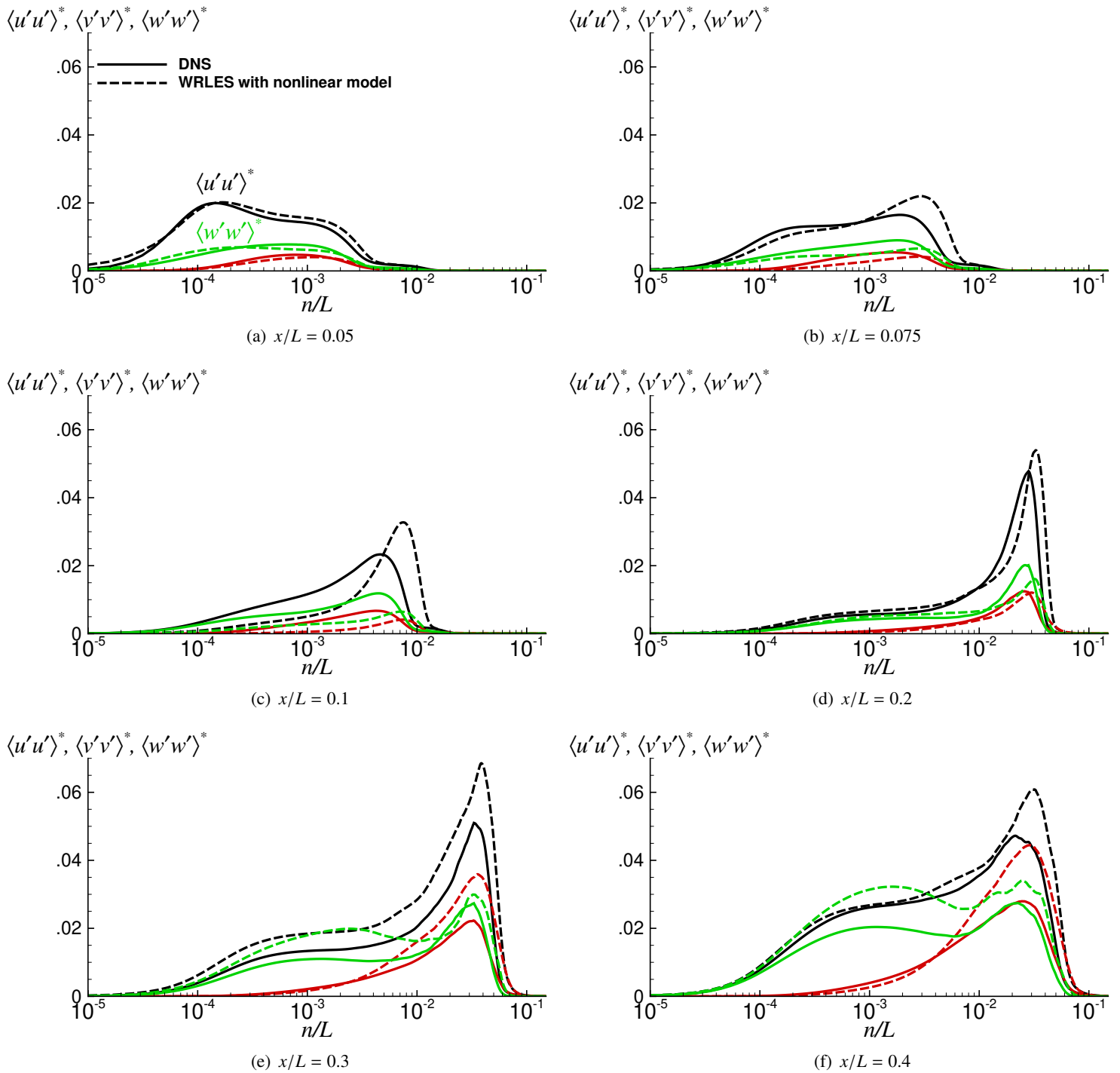

Figure 8. Normal Reynolds stress profiles in the region where $0.05 \leq x/L \leq 0.4$.
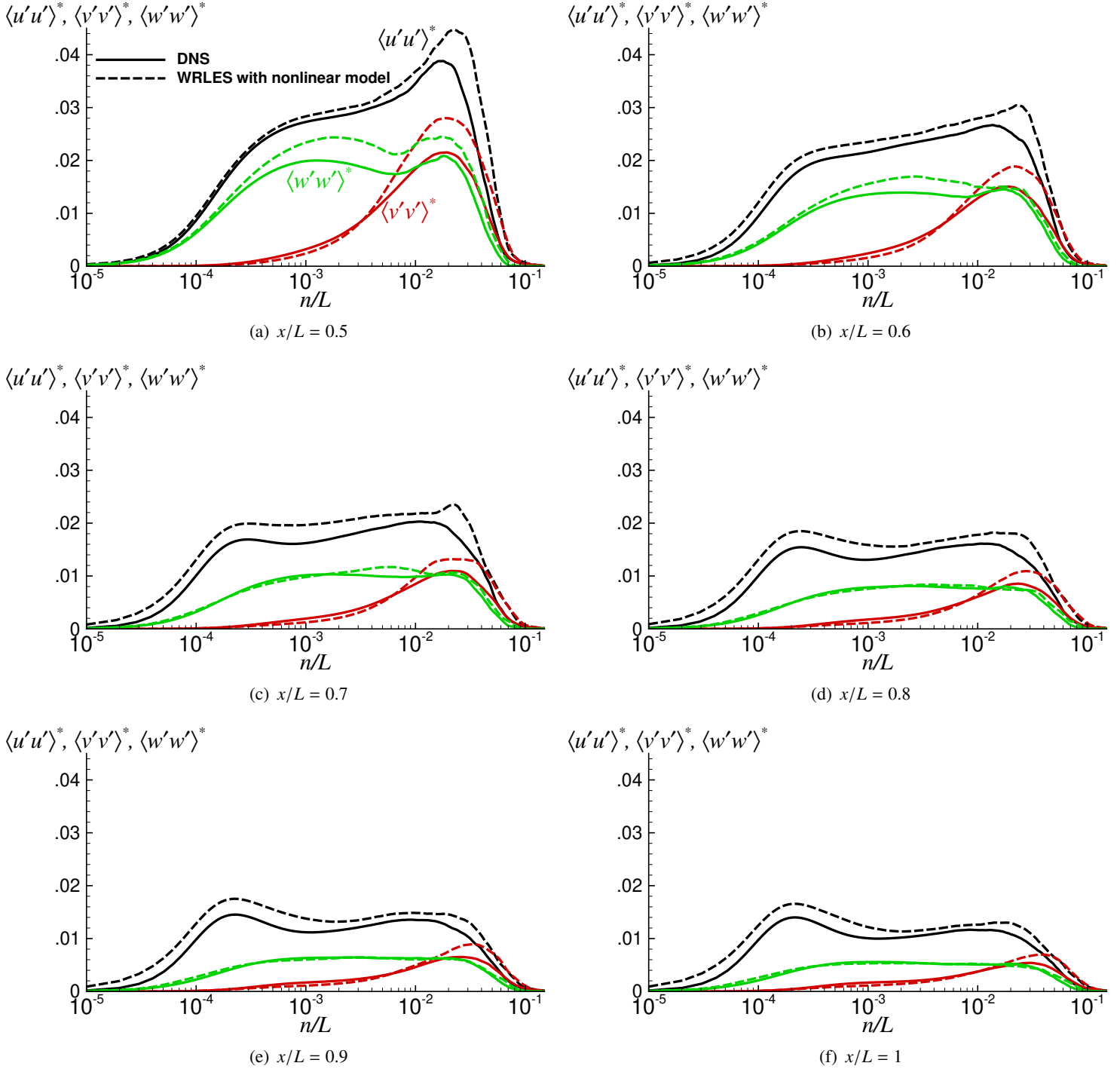
Figure 9. Normal Reynolds stress profiles in the region $0.5 \leq x/L \leq 1$.

The proposed model was tested in a spanwise-periodic computation of a turbulent flow past a Gaussian bump, also known as the speed bump flow, for a Reynolds number of 170000 based on the bump height (or 2 million based on the experimental model width), using a grid containing about 659 million points. The predictions obtained with the proposed model are found to be much improved when compared to those obtained on the same grid with no model (i.e., implicit large-eddy simulation) and with the Vreman model,

which is a linear eddy-viscosity model, in addition to the results from several other alternative nonlinear model formulations that were considered. Further comparisons with the results available from an earlier higher-fidelity simulation of the problem under the same conditions, performed using a grid of 10.2 billion grid points, showed that the proposed model can predict the flow development within the accelerating region over the windward side of the bump with reasonable success, but better quantitative agreement with the DNS is desirable. In particular, the mean velocity and total Reynolds shear stress profiles in the late stages of acceleration are predicted by the proposed nonlinear model more accurately than other models. The mean flow response to the adverse pressure gradient past the apex over the leeward side of the bump is slightly faster than that observed in the higher-fidelity simulation, with related effects observed on the Reynolds stress profile behavior in the same region. This then leads to a slightly early separation point and alters the initial conditions of the separated flow, causing other differences in the separation region relative to the results from the higher-fidelity simulation. The separated shear layer generates higher levels of peak TKE and Reynolds stress levels in the WRLES, and the reversed flow region is also relatively stronger than that in the DNS. Despite such differences, reasonable overall similarity is found in much of the separation region and the recovery zone downstream of separation. The comparisons with the DNS data show promising success for the proposed model.

It is hoped that the dynamic evaluation of the production and destruction term coefficients in the ε_{sgs} transport equation, or more advanced dissipation models that can be used in the closure of the k_{sgs} transport equation without the need to solve a separate transport equation for ε_{sgs}, will be able to rectify the identified shortcomings of the model. Our experience during the course of this work indicates that the simple dissipation model derived from dimensional analysis will not suffice in a complex problem such as the speed bump flow. The turbulent channel flow results shown in Appendix A, which were obtained by solving the transport equation of the specific dissipation rate, ω_{sgs}, rather than ε_{sgs}, provide further evidence for the potential of the proposed nonlinear model when the transport equation for k_{sgs} is provided with a proper dissipation closure.

For the chosen grid size, the proposed model was found to provide the best overall results for the problem under investigation, among the three models tested during the course of this study. Implementation of this model into the flow solver increases the computational cost per time step by a factor about two, relative to the cost of ILES with no explicit SGS model. When compared to the higher-fidelity simulation performed on 10.2 billion grid points with the same time step, the proposed model on the coarsened grid reduces the computational cost by a factor of about 8. Further reduction of the computational cost of the speed bump WRLES should be possible by coarsening of the vertical grid spacings in the region away from the wall.

Acknowledgments

Appendix A: Application to Turbulent Channel Flow

To further evaluate the performance of the new nonlinear model, the turbulent channel flow problem was considered. The Reynolds number of the fully-developed turbulent channel flow is $Re_\tau = \rho_{bulk} u_\tau h / \mu_{wall} = 590$, where ρ_{bulk} is the bulk density, u_τ is the wall friction velocity, h is the channel half-height and μ_{wall} is the viscosity on the wall. The domain size is $2\pi h$ in the streamwise direction, x, $2h$ in the wall-normal

26

direction, y, and πh in the spanwise direction, z. The flow is periodic both in the streamwise and spanwise directions and is bounded by solid walls at $y = 0$ and $2h$. Because of the imposed streamwise periodicity, a source term is added to the streamwise momentum and energy equations to drive the flow at a constant mass flow rate. The Mach number based on bulk velocity and sound speed on the wall is set to 0.2.

The grid used for the LES contains $193 \times 129 \times 193$ points along x, y and z directions, respectively. The grid resolution in wall units is $\Delta x^+ \approx 20$ in the streamwise direction and $\Delta z^+ \approx 10$ in the spanwise direction. In the vertical direction, $\Delta y^+ \approx 1$ on the wall and $\Delta y^+ \approx 10$ at the channel centerline. These streamwise and spanwise resolutions are about two to four times coarser than those used for DNS at the same Re_τ using spectral methods [58, 59]. The resolutions along the vertical direction are generally coarser by a factor of two relative to the DNS, except very near the wall, where Δy^+ values much smaller than 1 can be found when spectral methods are employed for the DNS. For the time integration, the second-order implicit scheme is used, with a maximum Courant-Friedrichs-Lewy (CFL) number of about 2.5. To ensure full convergence of the time-averaged results, the flow statistics are averaged over $1589 h / u_{bulk}$.

The transport equations solved for this case are given by

$$\frac{\partial \overline{\rho} k_{sgs}}{\partial t} + \frac{\partial \overline{\rho} \tilde{u}_i k_{sgs}}{\partial x_i} = -\tau_{ij} \widetilde{S}_{ij} + \frac{\partial}{\partial x_i} \left[\left(\tilde{\mu} + \frac{\mu_t}{\sigma_k} \right) \frac{\partial k_{sgs}}{\partial x_i} \right] - \beta^* \overline{\rho} k_{sgs} \omega_{sgs} , \quad (36)$$

$$\frac{\partial \overline{\rho} \omega_{sgs}}{\partial t} + \frac{\partial \overline{\rho} \tilde{u}_i \omega_{sgs}}{\partial x_i} = -\alpha \frac{\omega_{sgs}}{k_{sgs}} \tau_{ij} \widetilde{S}_{ij} + \frac{\partial}{\partial x_i} \left[\left(\tilde{\mu} + \frac{\mu_t}{\sigma_\omega} \right) \frac{\partial \omega_{sgs}}{\partial x_i} \right] - \beta \overline{\rho} \omega_{sgs}^2 , \quad (37)$$

where ω_{sgs} is the specific dissipation rate that is related to ε_{sgs} as $\varepsilon_{sgs} = \beta^* k_{sgs} \omega_{sgs}$. The coefficients in the above equations are taken as $\sigma_k = \sigma_\omega = 2$, $\alpha = 5/9$, $\beta = 3/40$, and $\beta^* = 9/100$, which are the same as the Wilcox-1988 $k - \omega$ model coefficients [43]. While the later versions of the Wilcox $k - \omega$ models (1998 and 2006) specify slightly different coefficient values in combination with elaborate auxiliary functions aimed for better performance in free shear layers, we prefer to use the coefficients from the simplest version without any blending functions. The wall boundary conditions for k_{sgs} and ω_{sgs} are set as

$$k_{sgs} = 0 , \quad \omega_{sgs} = 10 \frac{6 \tilde{\mu} / \overline{\rho}}{\beta (\Delta y_1)^2} , \quad (38)$$

where Δy_1 is the vertical distance between the wall point and the first point off the wall. This wall boundary condition for ω_{sgs} originates from Menter's work on the $k - \omega$ model [60]. As noted in section 2, in wall-bounded flows, the $k - \omega$ model is superior to the $k - \varepsilon$ model near the wall and does not require near-wall damping functions, but is known to be very sensitive to the freestream value of ω in free shear layers [42]. However, this weakness of the $k - \omega$ model is not an issue in the turbulent channel flow; hence, the use of ω_{sgs} over ε_{sgs} is justifiable for this particular test case given its aforementioned advantages.

Figure 10 compares our mean streamwise velocity and Reynolds stress component profiles with those from Moser et al. [58] as well as Vreman and Kuerten [59]. These researchers used spectral methods to perform an incompressible DNS at the same Re_τ. In the figure, $u'u', v'v', w'w'$ and $u'v'$ represent the streamwise, wall-normal, spanwise and shear components of the Reynolds stress, respectively. For the WRLES, the shown Reynolds stress components are the total quantities, which are obtained by adding up the resolved and modeled components. The comparisons show a very good agreement with the DNS results, with relatively small differences. These results provide further evidence for the potential of the proposed nonlinear model when the transport equation for k_{sgs} is provided with a proper dissipation closure.
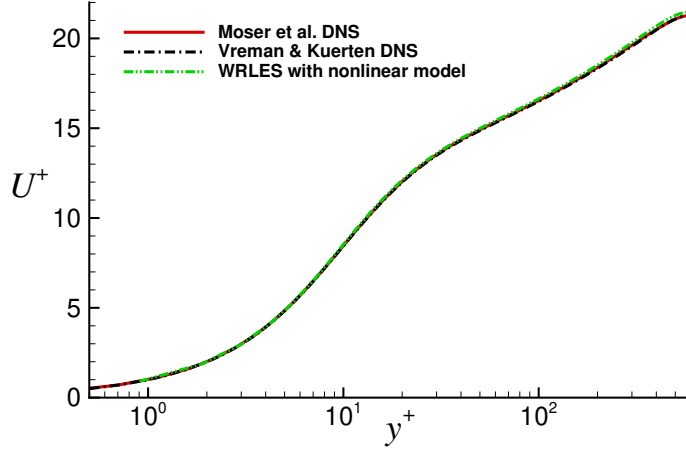
(a) Mean velocity
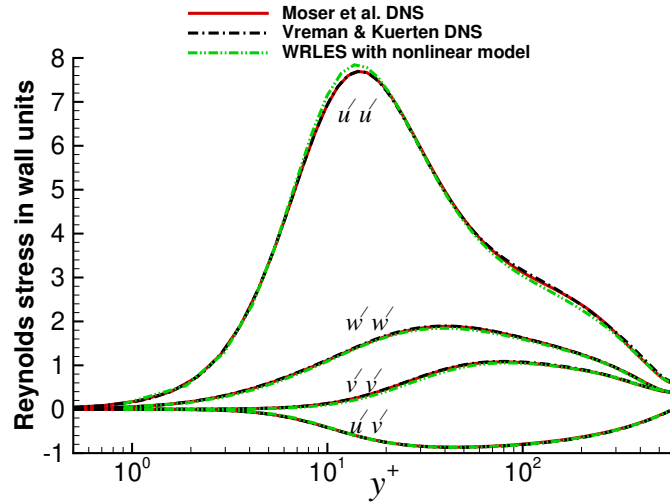
(b) Reynolds stress components

Figure 10. Turbulent channel flow mean streamwise velocity and Reynolds stresses in wall units.

Appendix B: Alternative Model Formulation Without Transport Equations

An alternative formulation of the nonlinear model does not include the transport equations for k_{sgs} and its dissipation rate, but employs a simple model based on the scale-similarity assumption to model k_{sgs}. The details of the simpler model formulation, and a summary of the results obtained with it are presented here.

The alternative model, instead of Eq. (3), is of the following form

$$\tau_{ij} - \frac{2}{3}\overline{\rho}k_{sgs}\delta_{ij} = C_1\left(L_{ij}^m - \frac{\delta_{ij}}{3}L_{kk}^m\right) + C_2\frac{L_{kk}^m}{|\widetilde{M}|}\widetilde{M}_{ij} + C_3\frac{L_{kk}^m}{|\widetilde{N}|}\widetilde{N}_{ij}, \tag{39}$$

where

$$L_{ij}^m = \widehat{\overline{\rho\tilde{u}_i\tilde{u}_j}} - \frac{\widehat{\overline{\rho}\tilde{u}_i}\,\widehat{\overline{\rho}\tilde{u}_j}}{\widehat{\overline{\rho}}} \,, \quad \widehat{M}_{ij} = \widehat{S}_{ik}\widehat{S}_{kj} - \frac{\delta_{ij}}{3}\widehat{S}_{kl}\widehat{S}_{kl} \,, \quad \widehat{N}_{ij} = \widehat{S}_{ik}\widehat{\Omega}_{kj} - \widehat{\Omega}_{ik}\widehat{S}_{kj} \,, \tag{40}$$

$$|\widehat{M}| = \left(\widehat{M}_{ij}\widehat{M}_{ij}\right)^{1/2} \,, \quad |\widehat{N}| = \left(\widehat{N}_{ij}\widehat{N}_{ij}\right)^{1/2} \,, \quad \widehat{S}_{ij} = \frac{1}{2}\left(\frac{\partial\tilde{u}_i}{\partial x_j} + \frac{\partial\tilde{u}_j}{\partial x_i}\right) \,, \quad \widehat{\Omega}_{ij} = \frac{1}{2}\left(\frac{\partial\tilde{u}_i}{\partial x_j} - \frac{\partial\tilde{u}_j}{\partial x_i}\right) \,. \tag{41}$$

The model is derived under the same assumptions discussed in section 2. The solution of the following 3×3 linear system provides the three model coefficients

$$\begin{bmatrix} \mathscr{L}_{ij}^d\mathscr{L}_{ij}^d & \mathscr{L}_{ij}^d\gamma_{ij} & \mathscr{L}_{ij}^d\lambda_{ij} \\[2mm] \gamma_{ij}\mathscr{L}_{ij}^d & \gamma_{ij}\gamma_{ij} & \gamma_{ij}\lambda_{ij} \\[2mm] \lambda_{ij}\mathscr{L}_{ij}^d & \lambda_{ij}\gamma_{ij} & \lambda_{ij}\lambda_{ij} \end{bmatrix} \begin{bmatrix} C_1 \\[2mm] C_2 \\[2mm] C_3 \end{bmatrix} = \begin{bmatrix} L_{ij}^d\mathscr{L}_{ij}^d \\[2mm] L_{ij}^d\gamma_{ij} \\[2mm] L_{ij}^d\lambda_{ij} \end{bmatrix} \tag{42}$$

where

$$L_{ij}^d = L_{ij}^m - \frac{\delta_{ij}}{3}L_{kk}^m \,, \quad \mathscr{L}_{ij}^d = \mathscr{L}_{ij}^m - \frac{\delta_{ij}}{3}\mathscr{L}_{kk}^m \,, \quad \gamma_{ij} = \frac{\mathscr{L}_{kk}^m}{|\widetilde{\widehat{M}}|}\widetilde{\widehat{M}}_{ij} \,, \quad \lambda_{ij} = \frac{\mathscr{L}_{kk}^m}{|\widetilde{\widehat{N}}|}\widetilde{\widehat{N}}_{ij} \,, \tag{43}$$

$$\mathscr{L}_{ij}^m = \widetilde{\widehat{\overline{\rho}\hat{\tilde{u}}_i\hat{\tilde{u}}_j}} - \frac{\widetilde{\overline{\rho}\hat{\tilde{u}}_i}\,\widetilde{\overline{\rho}\hat{\tilde{u}}_j}}{\widetilde{\widehat{\overline{\rho}}}} \,, \quad \hat{\tilde{u}}_i = \frac{\widehat{\overline{\rho}\tilde{u}_i}}{\widehat{\overline{\rho}}} \,, \quad \widetilde{\widehat{M}}_{ij} = \widetilde{\widehat{S}}_{ik}\widetilde{\widehat{S}}_{kj} - \frac{\delta_{ij}}{3}\widetilde{\widehat{S}}_{kl}\widetilde{\widehat{S}}_{kl} \,, \quad \widetilde{\widehat{N}}_{ij} = \widetilde{\widehat{S}}_{ik}\widetilde{\widehat{\Omega}}_{kj} - \widetilde{\widehat{\Omega}}_{ik}\widetilde{\widehat{S}}_{kj} \,, \tag{44}$$

$$|\widetilde{\widehat{M}}| = \left(\widetilde{\widehat{M}}_{ij}\widetilde{\widehat{M}}_{ij}\right)^{1/2} \,, \quad |\widetilde{\widehat{N}}| = \left(\widetilde{\widehat{N}}_{ij}\widetilde{\widehat{N}}_{ij}\right)^{1/2} \,, \quad \widetilde{\widehat{S}}_{ij} = \frac{1}{2}\left(\frac{\partial\hat{\tilde{u}}_i}{\partial x_j} + \frac{\partial\hat{\tilde{u}}_j}{\partial x_i}\right) \,, \quad \widetilde{\widehat{\Omega}}_{ij} = \frac{1}{2}\left(\frac{\partial\hat{\tilde{u}}_i}{\partial x_j} - \frac{\partial\hat{\tilde{u}}_j}{\partial x_i}\right) \,. \tag{45}$$

In the model formulation, the first filtering operation denoted by $\widehat{(\ )}$ has a width of $m\Delta$, while the second filtering operation denoted by $\widetilde{(\ )}$ has a larger width, $n\Delta$, where $n > m$ and Δ is the local grid spacing. As discussed in section 2, $n/m = m/\ell$, where $\ell = 1.7$ for the fourth-order accurate spatial discretization scheme used in this work. We set $n = 6$, which gives $m \approx 3.19$.

To model $\overline{\rho}k_{sgs} = \tau_{kk}/2$ without solving a transport equation, one could use the simple Yoshizawa model [61] expressed as $\tau_{kk} = C_I\overline{\rho}\overline{\Delta}^2\left(2\widetilde{S}_{ij}\widetilde{S}_{ij}\right)$ and determine the model coefficient dynamically. However, this formulation involves the characteristic length scale, $\overline{\Delta}$, which we prefer not to use for the reason mentioned in section 2. We instead propose the following scale-similarity based relation to model τ_{kk}, with

$$\tau_{kk} = C_I L_{kk}^m = C_I\left(\widehat{\overline{\rho\tilde{u}_k\tilde{u}_k}} - \frac{\widehat{\overline{\rho}\tilde{u}_k}\,\widehat{\overline{\rho}\tilde{u}_k}}{\widehat{\overline{\rho}}}\right) \,, \tag{46}$$

and assume that it is also valid at a larger scale, which then leads to $T_{kk} = C_I H_{kk}$, where

$$T_{ij} = \widehat{\overline{\rho u_i u_j}} - \frac{\widehat{\overline{\rho}u_i}\,\widehat{\overline{\rho}u_j}}{\widehat{\overline{\rho}}} \,, \quad H_{ij} = \widetilde{\widehat{\overline{\rho}\hat{u}_i\hat{u}_j}} - \frac{\widetilde{\overline{\rho}\hat{u}_i}\,\widetilde{\overline{\rho}\hat{u}_j}}{\widetilde{\widehat{\overline{\rho}}}} \,. \tag{47}$$

Further assuming that this expression holds true after replacing u_i with $\tilde{u}_i$, and ρ with $\overline{\rho}$ in T_{kk} and H_{kk}, gives

$$L_{kk}^m = C_I\mathscr{L}_{kk}^m = C_I\left(\widetilde{\widehat{\overline{\rho}\hat{\tilde{u}}_k\hat{\tilde{u}}_k}} - \frac{\widetilde{\overline{\rho}\hat{\tilde{u}}_k}\,\widetilde{\overline{\rho}\hat{\tilde{u}}_k}}{\widetilde{\widehat{\overline{\rho}}}}\right) \,. \tag{48}$$

We therefore obtain $C_I = L_{kk}^m / \mathcal{L}_{kk}^m$, which can be used to compute $\bar{\rho} k_{sgs} = \tau_{kk}/2 = 0.5 C_I L_{kk}^m$.

As the model naturally allows backscatter, determination of the model coefficients using a least-squares error approach might lead to locally excessive backscatter, which could then be a potential source of numerical instability. The more sophisticated model formulation discussed in section 2, which includes a transport equation for k_{sgs}, is specifically aimed at resolving this issue, but comes with increased computational cost. In the revised formulation, any backscatter generated by the model appears as a negative production term in the transport equation, and this leads to a reduction in the local k_{sgs}. If the backscatter persists, the local k_{sgs} will tend toward zero, and this will terminate the backscatter. Thus, in the revised model, backscatter can occur only over a finite period, which enables the model to automatically stabilize itself.

To limit the amount of backscatter and maintain numerical stability with the simpler model formulation, the backscatter amount could be constrained not to exceed several times the local value of the resolved viscous dissipation. We anticipate that the maximum stable ratio between backscatter and resolved viscous dissipation would be sensitive to the grid resolution, numerical discretization as well as specific problem details among other factors, and can be adjusted via numerical experimentation. The energy flux from the resolved to the unresolved scales is given by $\Pi = -\tau_{ij} \widetilde{S}_{ij}$. Here, $\Pi \geq 0$ means forward scatter, otherwise backscatter occurs. The resolved viscous dissipation is $\Phi = \widetilde{\sigma}_{ij} \widetilde{S}_{ij} \geq 0$, where $\widetilde{\sigma}_{ij}$ is the resolved viscous stress tensor. The limiter on the backscatter amount is imposed by multiplying τ_{ij} with a scalar factor, β, which is defined as

$$\beta = \begin{cases} 1 & \text{if } \Pi \geq 0 \\ \min\left[1, -\alpha\left(\Phi/\Pi\right)\right] & \text{if } \Pi < 0, \end{cases} \tag{49}$$

where $\alpha = 3$ for the present study. This value is chosen to ensure numerical stability over long run intervals. To our knowledge, this type of backscatter control was first proposed by Abbà et al. [62], who used $\alpha = 1$ in their study. With the present limiter, all model coefficients are scaled by $\beta < 1$ in order to satisfy the backscatter constraint. Other than this rescaling, no other procedure, such as spatial/temporal averaging or clipping of the coefficients, is performed. Implementation of the alternative model in the present study increases the computational cost per time step by about 40%, relative to the cost of ILES. When compared to the DNS performed on 10.2 billion grid points with the same time step, the alternative model on the present grid that contains about 659 million points, reduces the computational cost by a factor of 11.

We now examine the speed bump flow results obtained with the simpler alternative model formulation and compare them with the earlier DNS [5]. The statistical data obtained with the alternative model were time averaged over $11L/U_\infty$, same as that for the DNS. Figure 11 provides the C_p and C_f distributions. The overall agreement of the C_f distribution between the DNS and WRLES with the alternative model is quite good, except for the slight delay in the separation point. The corresponding agreement in the C_p distribution is also reasonable, but the C_p plateau in the WRLES is lower compared to the DNS. This is because of the relatively weaker separation in the WRLES with the alternative model and other related differences in the development of the separated flow, which will be more evident shortly.

Figure 12 depicts the mean streamwise velocity, total Reynolds shear stress, and total TKE profile comparisons on the windward side of the bump. The response of the mean streamwise velocity profile to the adverse and favorable pressure gradients encountered in that region, and the associated changes in the Reynolds shear stress and TKE profiles, are captured significantly better by this alternative model when compared to the revised formulation results in the same region, presented earlier in Figure 3. Relative to the DNS, the near-wall Reynolds shear stress peak within the emerging internal layer in the WRLES is slightly more energetic at $x/L = -0.1$, while the agreement with the DNS is very good at the apex. The TKE distributions with the alternative model also show reasonable agreement with the DNS, but the TKE peak tends to be generally overpredicted, particularly at the last two stations. The near-wall TKE levels at these two stations are also found to be higher with the alternative model. Despite such differences, the overall agreement with the DNS over the windward side of the bump is deemed satisfactory and generally better than that achieved

30

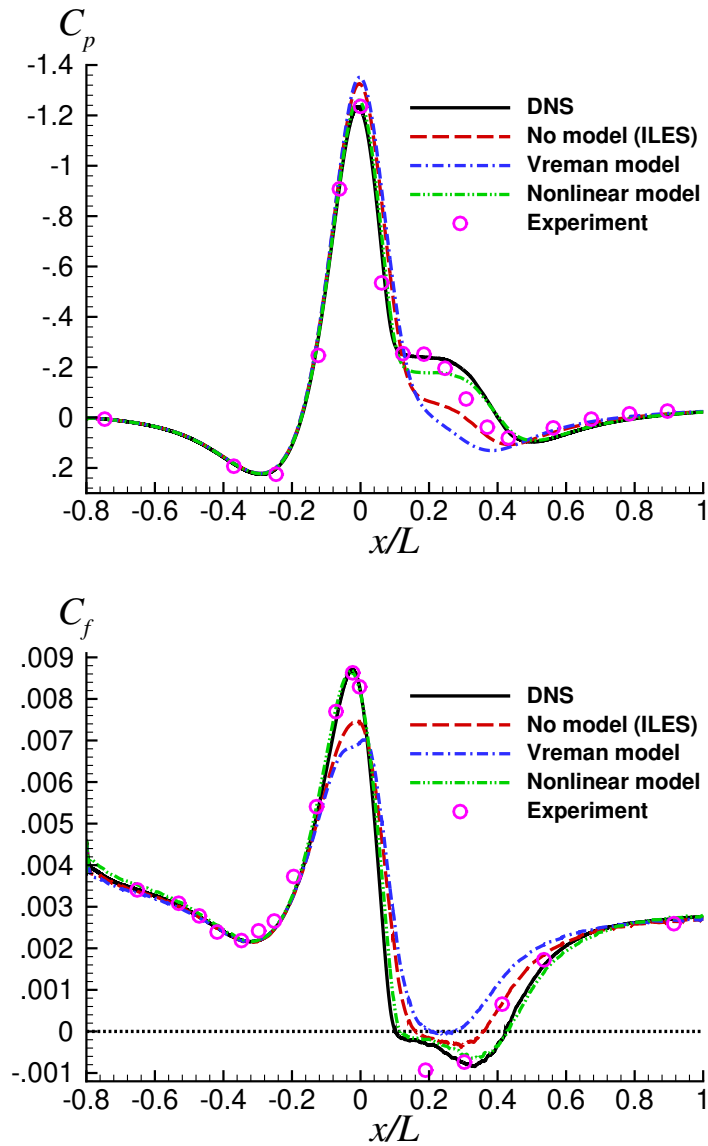with the revised model formulation in the same region.

Figure 11. C_p and C_f distributions.

Examination of the profiles in the deceleration and separation region, depicted in Figure 13, shows important differences between the DNS and the WRLES with the alternative model. The mean velocity profile response to the adverse pressure gradient immediately past the apex over the leeward side of the bump in the WRLES, as shown by the first two stations in Figure 13 is not as rapid as that observed in the DNS. This slower response of the mean velocity profile in the WRLES hampers the development of the Reynolds shear stress and TKE profiles. The flow separation occurs at about $x/L = 0.1$ in the DNS and at $x/L \approx 0.118$ in the WRLES. Such differences in the deceleration region between the two cases affect what happens within the separation zone. The profile comparisons at $x/L = 0.15$ and 0.2 reveal the subsequent differences between the two cases in the early stages of separation. The TKE peak within the free shear layer is considerably stronger in the DNS; this is related to the faster shear layer evolution in that case. Despite the somewhat lower Reynolds shear stress peak at $x/L = 0.15$ in the DNS, that peak surpasses that of the
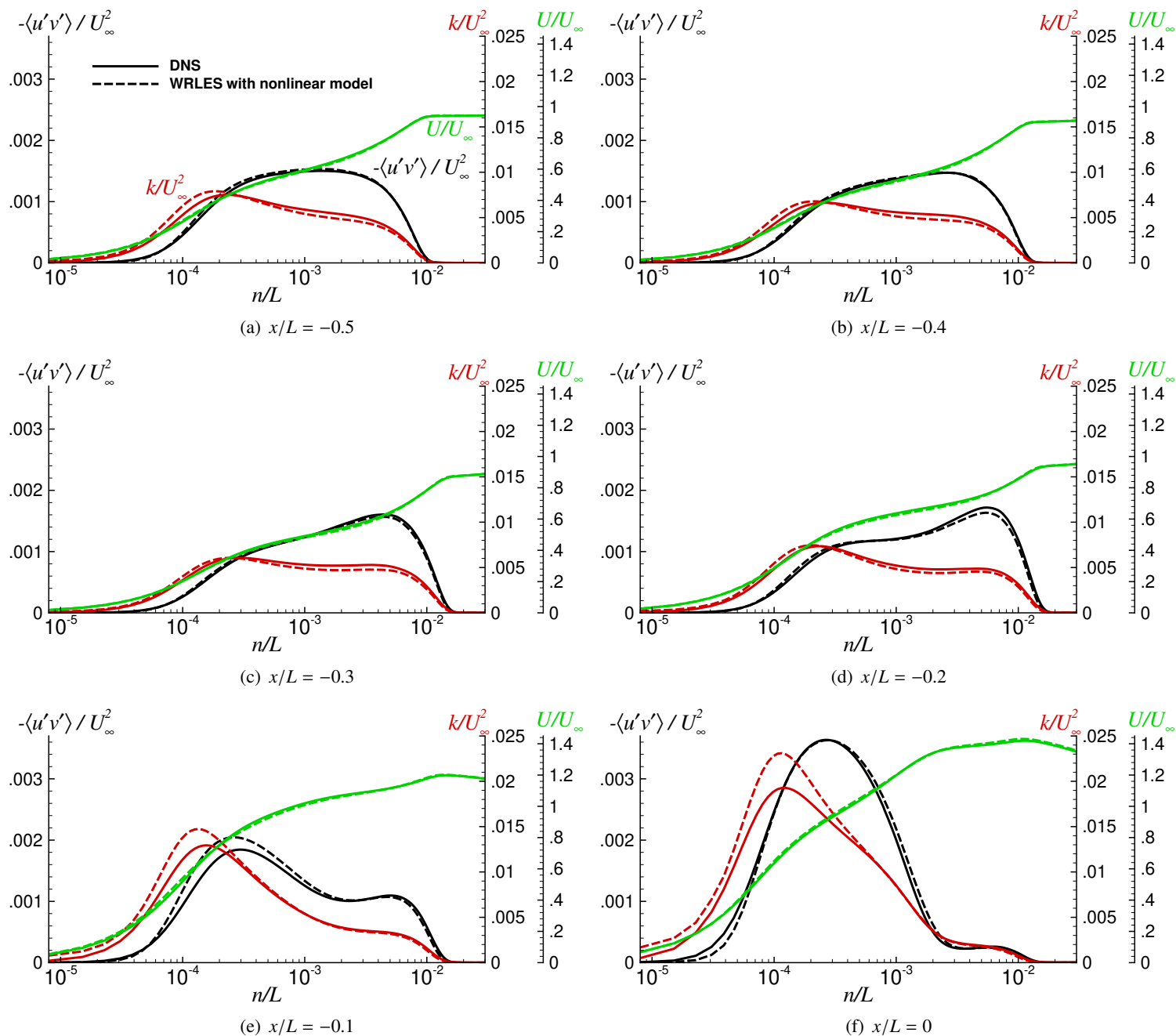
WRLES in the later stages of separation.

(a) $x/L = -0.5$

(b) $x/L = -0.4$

(c) $x/L = -0.3$

(d) $x/L = -0.2$

(e) $x/L = -0.1$

(f) $x/L = 0$

Figure 12. Wall-normal profiles in the region where $-0.5 \leq x/L \leq 0$.

At $x/L = 0.3$ and 0.4, which correspond to the middle and late stages of separation, the velocity profiles are fairly close to one another, but the differences in the Reynolds shear and TKE profiles continue to persist. The TKE and Reynolds shear stress peaks found within the free shear layer are relatively weaker in the WRLES, when compared to the DNS. This is likely an artifact of the backscatter limiter used in the alternative model formulation, which is needed to maintain numerical stability. The limiter appears to have been somehow too restrictive in the separated region. Rather than setting a constant ratio between the

allowed backscatter and the resolved viscous dissipation throughout the entire flowfield, that value could be allowed to vary in space depending on local flow conditions; however, despite our best attempts, we have been unable to develop a robust dynamic procedure for that purpose.
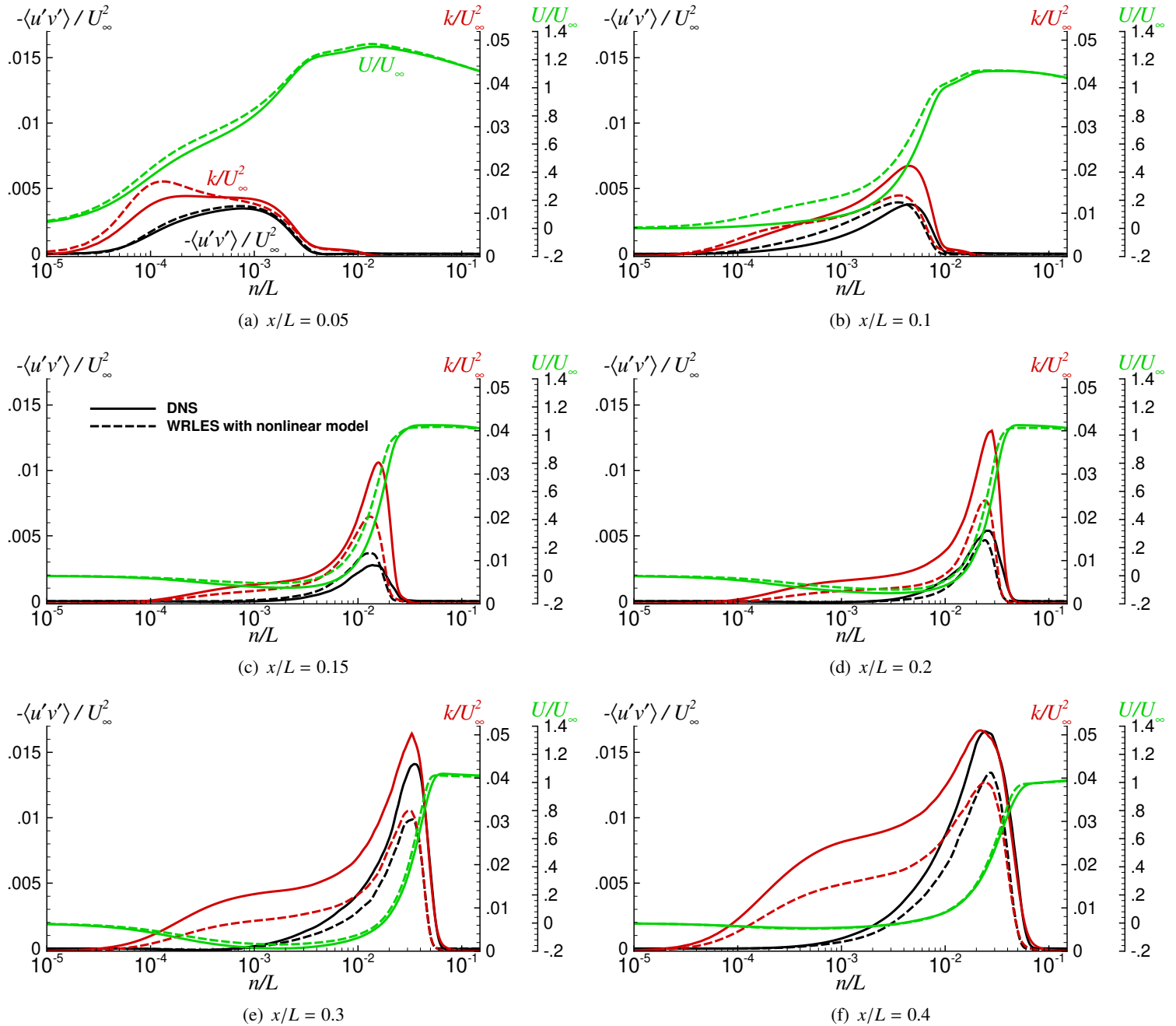

Figure 13. **Wall-normal profiles in the region where $0.05 \leq x/L \leq 0.4$.**

The DNS also shows considerably higher TKE levels in the recirculating flow region between the free shear layer and the wall, which is an outcome of the stronger reversed flow in the DNS. The stronger reversed flow in the DNS, in turn, is correlated with the higher peak TKE levels generated within the free shear layer. The flow reattachment is at $x/L \approx 0.423$ and 0.427 in the DNS and the WRLES with the

alternative model, respectively. Relative to the DNS, the error in the length of separation region is about 4% with the simpler alternative model, and about 8% with the revised model. The profiles taken within the recovery zone following separation, depicted in Figure 14, show that the differences between the two simulations diminish as we move further downstream. Reasonable agreement between the two simulations is again found in the later stages of the recovery zone. The normal Reynolds stress component profiles obtained with the alternative model generally mirror the noted similarities and the differences compared to the DNS, and are omitted here for brevity.
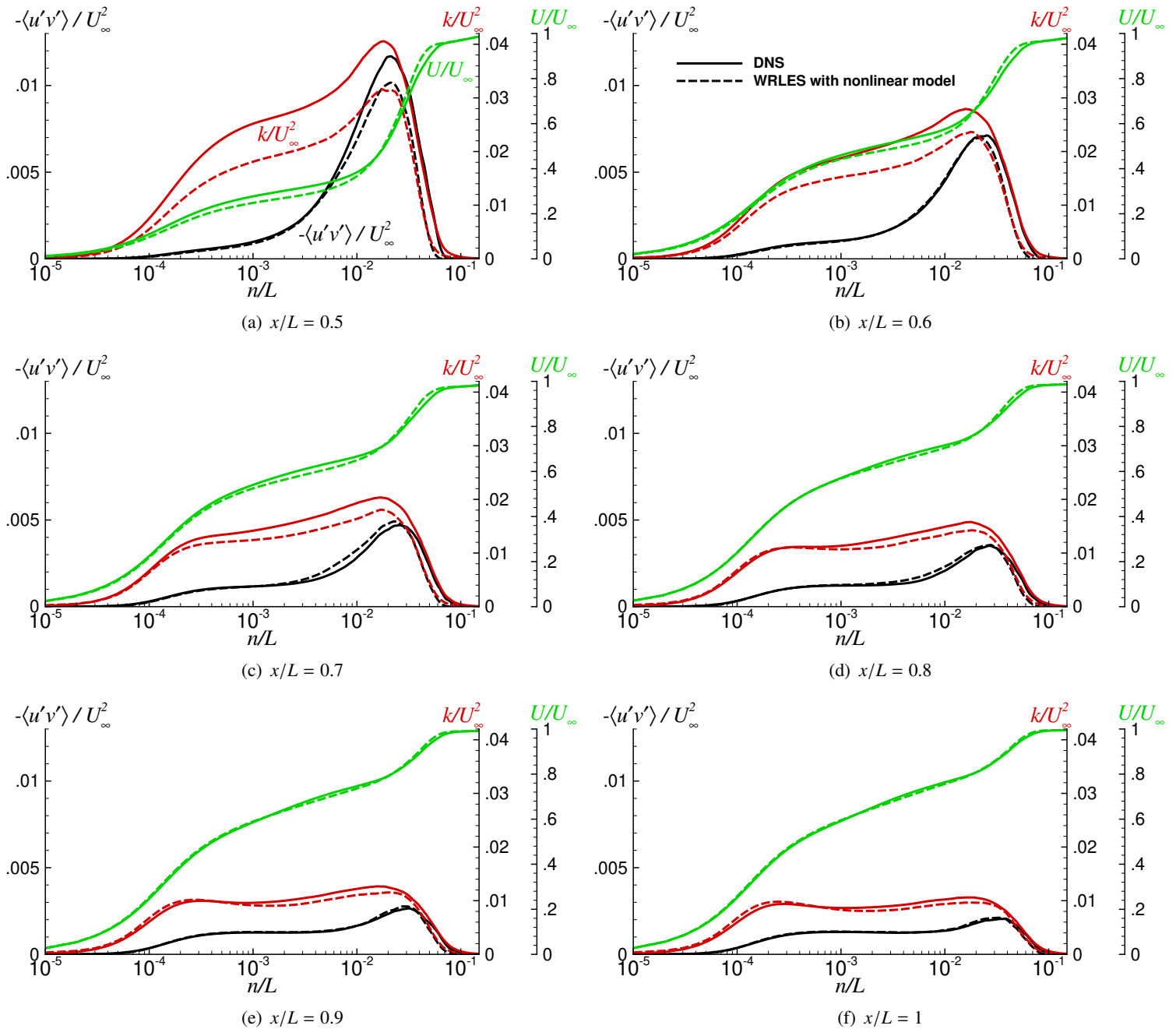

Figure 14. **Wall-normal profiles in the region where $0.5 \leq x/L \leq 1$.**

Figure 15(a) shows the mean velocity and the total Reynolds shear stress profiles from the WRLES with the alternative model at the bump apex where $x/L = 0$, and the comparison against the other data. We see that the mean velocity and the Reynolds shear stress peak profiles obtained with the alternative model show the best agreement with the DNS, when compared against the results obtained with ILES and the Vreman model. The alternative nonlinear model profiles are also relatively better than those obtained with the revised formulation, shown earlier in Figure 6(a). Figure 15(b) shows the mean velocity and the total Reynolds shear stress profiles at $x/L = 0.25$, which is located in the middle of the separation region, and the comparison against the other data. The mean velocity profile obtained with the alternative model shows reasonable agreement with the DNS result. Because of the relatively weaker flow separation with the alternative model, the Reynolds shear stress peak is weaker compared to the DNS. In contrast, the revised model formulation generates a stronger separation and thus a higher Reynolds shear stress peak at the same station, as seen earlier in Figure 6(b).
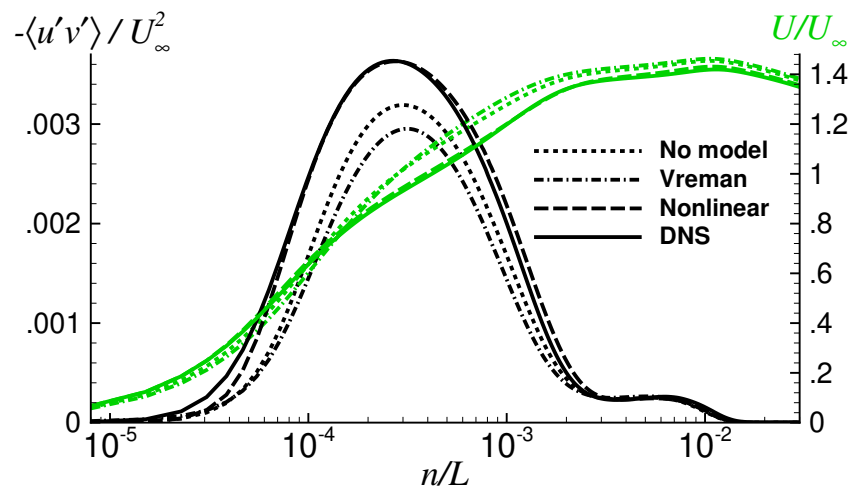
(a) $x/L = 0$
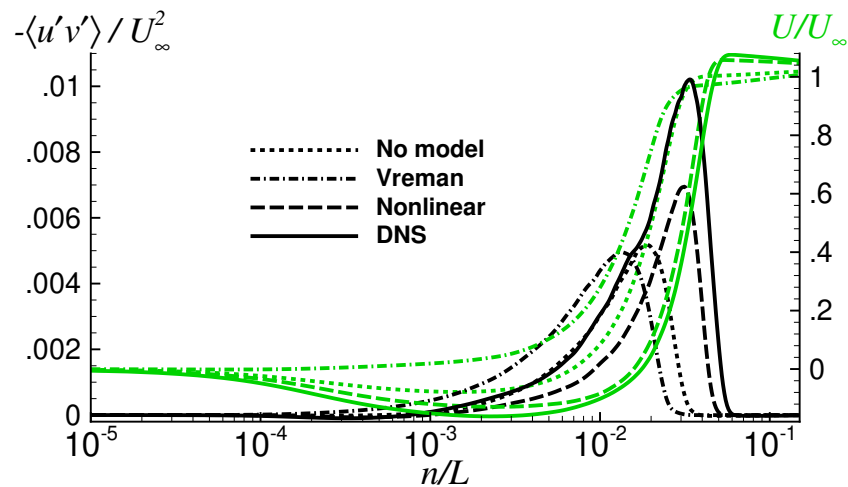
(b) $x/L = 0.25$

Figure 15. Comparison of the mean velocity and total Reynolds shear stress profiles.

In conclusion, the simpler alternative model formulation gives improved predictions relative to the revised model formulation over the windward side of the bump, but displays some discrepancies relative to the DNS over the leeward side, which are believed to be due to the restrictive nature of the backscatter

limiter in that region. Altogether, the predictions obtained with the revised formulation over the leeward side of the bump can be considered better than those obtained with the simpler model. As noted earlier, the revised formulation eliminates the backscatter limiter needed in the simpler formulation, but requires the solution of two transport equations, one for the subgrid kinetic energy, and another one for its dissipation rate. Both model formulations have strengths and deficiencies, which may be rectified through future enhancements. Nevertheless, in their present form, the simpler version could be an attractive model for attached flows subjected to pressure gradient and surface curvature effects without undergoing separation, while the revised version seems more suitable for flows involving separation, as well as free shear layers. Further improvements to both model formulations are highly desirable.

References

[1] Slotnick, J. P., Integrated CFD Validation Experiments for Prediction of Turbulent Separated Flows for Subsonic Transport Aircraft, NATO Science and Technology Organization, Meeting Proceedings RDP, STO-MP-AVT-307, 2019.

[2] Iyer, P. S. and Malik, M. R., Wall-Modeled LES of Flow over a Gaussian Bump, AIAA Paper 2021-1438, AIAA SciTech 2021 Forum, Virtual Event, 2021.

[3] Prakash, A., Balin, R., Evans, J. A. and Jansen, K. E., Wall-Modeled Large Eddy Simulations of a Turbulent Boundary Layer over the Boeing Speed Bump at $Re_L = 2$ Million, AIAA Paper 2022-0338, AIAA SciTech 2022 Forum, San Diego, CA & Virtual Event, 2022.

[4] Whitmore, M. P., Griffin, K. P., Bose, S. T. and Moin, P., Large-Eddy Simulation of a Gaussian Bump with Slip-Wall Boundary Conditions, Annual Research Briefs 2021, Center for Turbulence Research, Stanford University, California, CA.

[5] Uzun, A. and Malik, M. R., High-Fidelity Simulation of Turbulent Flow Past Gaussian Bump, *AIAA Journal*, 2022, 60(4), 2130–2149.

[6] Williams, O., Samuell, M., Sarwas, S., Robbins, M. and Ferrante, A., Experimental Study of a CFD Validation Test Case for Turbulent Separated Flows, AIAA Paper 2020-0092, AIAA SciTech 2020 Forum, Orlando, Florida, 2020.

[7] Williams, O., Samuell, M., Robbins, M. L., Annamalai, H. and Ferrante, A., Characterization of Separated Flowfield over Gaussian Speed-Bump CFD Validation Geometry, AIAA Paper 2021-1671, AIAA SciTech 2021 Forum, Virtual Event, 2021.

[8] Gray, P., Gluzman, I., Thomas, F., Corke, T., Lakebrink, M. and Mejia, K., A New Validation Experiment for Smooth-Body Separation, AIAA Paper 2021-2810, AIAA Aviation 2021 Forum, Virtual Event, 2021.

[9] Gray, P., Gluzman, I., Thomas, F., Corke, T. and Mejia, K., Experimental Characterization of Smooth Body Flow Separation Over Wall-Mounted Gaussian Bump, AIAA Paper 2022-1209, AIAA SciTech 2022 Forum, San Diego, CA & Virtual Event, 2022.

[10] Vreman, A. W., An Eddy-Viscosity Subgrid-Scale Model for Turbulent Shear Flow: Algebraic Theory and Applications, *Physics of Fluids*, 2004, 16(10), 3670–3681.

[11] Uzun, A. and Malik, M. R., Large-Eddy Simulation of Flow over a Wall-Mounted Hump with Separation and Reattachment, *AIAA Journal*, 2018, 56(2), 715–730.

[12] Frohlich, J., Mellen, C. P., Rodi, W., Temmerman, L. and Leschziner, M. A., Highly Resolved Large-Eddy Simulation of Separated Flow in a Channel with Streamwise Periodic Constrictions, *Journal of Fluid Mechanics*, 2005, 526, 19–66.

[13] Bardina, J., Ferziger, J. H. and Reynolds, W. C., Improved Turbulence Models Based on Large Eddy Simulation of Homogeneous, Incompressible, Turbulent Flows, Report No. TF-19, Thermosciences Division, Department of Mechanical Engineering, Stanford University, Stanford, CA, 1983.

[14] Wilcox, D. C. and Rubesin, M. W., Progress in Turbulence Modeling for Complex Flow Fields Including Effects of Compressibility, NASA Technical Paper 1517, 1980.

[15] Lund, T. S. and Novikov, E. A., Parameterization of Subgrid-Scale Stress by the Velocity Gradient Tensor, Annual Research Briefs 1992, Center for Turbulence Research, Stanford University, California, CA.

[16] Kosović, B., Subgrid-Scale Modelling for the Large-Eddy Simulation of High-Reynolds-Number Boundary Layers, *Journal of Fluid Mechanics*, 1997, 336, 151–182.

[17] Heinz, S., Realizability of Dynamic Subgrid-Scale Stress Models via Stochastic Analysis, *Monte Carlo Methods and Applications*, 2008, 14(4), 311–329.

[18] Heinz, S. and Gopalan, H., Realizable versus Non-Realizable Dynamic Subgrid-Scale Stress Models, *Physics of Fluids*, 2012, 24(11), 115105.

[19] Wang, B.-C. and Bergstrom, D. J., A Dynamic Nonlinear Subgrid-Scale Stress Model, *Physics of Fluids*, 2005, 17, 035109.

[20] Speziale, C. G., Analytical Methods for the Development of Reynolds-Stress Closures in Turbulence, *Annual Review of Fluid Mechanics*, 1991, 23, 107–157.

[21] Rasam, A., Wallin, S., Brethouwer, G. and Johansson, A. V., Improving Separated-Flow Predictions using an Anisotropy-Capturing Subgrid-Scale Model, *International Journal of Heat and Fluid Flow*, 2017, 65, 246–251.

[22] Favre, A., Turbulence: Space-Time Statistical Properties and Behavior in Supersonic Flows, *Physics of Fluids*, 1983, 26(10), 2851–2863.

[23] Germano, M., A Proposal for a Redefinition of the Turbulent Stresses in the Filtered Navier–Stokes Equations, *Physics of Fluids*, 1986, 29(7), 2323–2324.

[24] Meneveau, C. and Katz, J., Scale-Invariance and Turbulence Models for Large-Eddy Simulation, *Annual Review of Fluid Mechanics*, 2000, 32(1), 1–32.

[25] Piomelli, U., Chapter Three - Large-Eddy Simulations, in: Durbin, P., ed., *Advanced Approaches in Turbulence*, Elsevier, 2021, 83–131.

[26] Ashcroft, G. and Zhang, X., Optimized Prefactored Compact Schemes, *Journal of Computational Physics*, 2003, 190(2), 459–477.

[27] Schumann, J.-E., Toosi, S. and Larsson, J., Assessment of Grid Anisotropy Effects on Large-Eddy-Simulation Models with Different Length Scales, *AIAA Journal*, 2020, 58(10), 4522–4533.

[28] Speziale, C. G., Galilean Invariance of Subgrid-Scale Stress Models in the Large-Eddy Simulation of Turbulence, *Journal of Fluid Mechanics*, 1985, 156, 55–62.

[29] Germano, M., Piomelli, U., Moin, P. and Cabot, W. H., A Dynamic Subgrid-Scale Eddy Viscosity Model, *Physics of Fluids A: Fluid Dynamics*, 1991, 3, 1760–1765.

[30] Lilly, D. K., A Proposed Modification of the Germano Subgrid-Scale Closure Method, *Physics of Fluids A: Fluid Dynamics*, 1992, 4(3), 633–635.

[31] Deardorff, J. W., The Use of Subgrid Transport Equations in a Three-Dimensional Model of Atmospheric Turbulence, *Journal of Fluids Engineering*, 1973, 95(3), 429–438.

[32] Schumann, U., Subgrid Scale Model for Finite Difference Simulations of Turbulent Flows in Plane Channels and Annuli, *Journal of Computational Physics*, 1975, 18(4), 376–404.

[33] Kim, W.-W. and Menon, S., A New Dynamic One-Equation Subgrid-Scale Model for Large Eddy Simulations, AIAA Paper 95-0356, 33rd Aerospace Sciences Meeting and Exhibit, Reno, NV, 1995.

[34] Kim, W.-W. and Menon, S., Application of the Localized Dynamic Subgrid-Scale Model to Turbulent Wall-Bounded Flows, AIAA Paper 97-0210, 35th Aerospace Sciences Meeting and Exhibit, Reno, NV, 1997.

[35] Nelson, C. C., *Simulations of Spatially Evolving Compressible Turbulence Using a Local Dynamic Subgrid Model*, Ph.D. thesis, School of Aerospace Engineering, Georgia Institute of Technology, Atlanta, GA, 1997.

[36] Wilcox, D. C., *Turbulence Modeling for CFD, Second Edition*, DCW Industries Inc., La Cañada, California, 2000, 123–125.

[37] Gallerano, F., Pasero, E. and Cannata, G., A Dynamic Two-Equation Sub Grid Scale Model, *Continuum Mechanics and Thermodynamics*, 2005, 17(2), 101–123.

[38] Hrenya, C. M., Bolio, E. J., Chakrabarti, D. and Sinclair, J. L., Comparison of Low Reynolds Number $k - \epsilon$ Turbulence Models in Predicting Fully Developed Pipe Flow, *Chemical Engineering Science*, 1995, 50(12), 1923–1941.

[39] Gaitonde, D. V. and Visbal, M. R., Padé-Type Higher-Order Boundary Filters for the Navier-Stokes Equations, *AIAA Journal*, 2000, 38(11), 2103–2112.

[40] Visbal, M. R. and Gaitonde, D. V., Very High-Order Spatially Implicit Schemes for Computational Acoustics on Curvilinear Meshes, *Journal of Computational Acoustics*, 2001, 9(4), 1259–1286.

[41] Wilcox, D. C., *Turbulence Modeling for CFD, Second Edition*, DCW Industries Inc., La Cañada, California, 2000, 119–122.

[42] Menter, F. R., Influence of Freestream Values on $k - \omega$ Turbulence Model Predictions, *AIAA Journal*, 1992, 30(6), 1657–1659.

[43] Wilcox, D. C., Reassessment of the Scale-Determining Equation for Advanced Turbulence Models, *AIAA Journal*, 1988, 26(11), 1299–1310.

[44] Moin, P., Squires, K., Cabot, W. and Lee, S., A Dynamic Subgrid-Scale model for Compressible Turbulence and Scalar Transport, *Physics of Fluids A: Fluid Dynamics*, 1991, 3(11), 2746–2757.

[45] Abe, K., An Improved Anisotropy-Resolving Subgrid-Scale Model with the Aid of a Scale-Similarity Modeling Concept, *International Journal of Heat and Fluid Flow*, 2013, 39, 42–52.

[46] Mokhtarpoor, R. and Heinz, S., Dynamic Large Eddy Simulation: Stability via Realizability, *Physics of Fluids*, 2017, 29(10), 105104.

[47] Shah, K. B., *Large Eddy Simulations of Flow Past a Cubic Obstacle*, Ph.D. thesis, Department of Mechanical Engineering, Stanford University, Stanford, CA, 1998.

[48] Lele, S. K., Compact Finite Difference Schemes with Spectral-Like Resolution, *Journal of Computational Physics*, 1992, 103(1), 16–42.

[49] Ekaterinaris, J. A., Implicit, High-Resolution, Compact Schemes for Gas Dynamics and Aeroacoustics, *Journal of Computational Physics*, 1999, 156(2), 272–299.

[50] Uzun, A., Hussaini, M. Y. and Streett, C. L., Large-Eddy Simulation of a Wing Tip Vortex on Overset Grids, *AIAA Journal*, 2006, 44(6), 1229–1242.

[51] Uzun, A. and Hussaini, M. Y., Investigation of High Frequency Noise Generation in the Near-Nozzle Region of a Jet Using Large Eddy Simulation, *Theoretical and Computational Fluid Dynamics*, 2007, 21(4), 291–321.

[52] Uzun, A. and Hussaini, M. Y., Simulation of Noise Generation in Near-Nozzle Region of a Chevron Nozzle Jet, *AIAA Journal*, 2009, 47(8), 1793–1810.

[53] Uzun, A. and Hussaini, M. Y., Prediction of Noise Generated by a Round Nozzle Jet Flow Using Computational Aeroacoustics, *Journal of Computational Acoustics*, 2011, 19(3), 291–316.

[54] Uzun, A. and Malik, M. R., Wall-Resolved Large-Eddy Simulations of Transonic Shock-Induced Flow Separation, *AIAA Journal*, 2019, 57(5), 1955–1972.

[55] Uzun, A. and Malik, M. R., Effect of Spatial Filtering in Implicit Large-Eddy Simulations of Separated Flows, *AIAA Journal*, 2019, 57(12), 5575–5581.

[56] Uzun, A. and Malik, M. R., Simulation of a Turbulent Flow Subjected to Favorable and Adverse Pressure Gradients, *Theoretical and Computational Fluid Dynamics*, 2021, 35(3), 293–329.

[57] Spalart, P. R. and Garbaruk, A. V., Correction to the Spalart-Allmaras Turbulence Model, Providing More Accurate Skin Friction, *AIAA Journal*, 2020, 58(5), 1903–1905.

[58] Moser, R. D., Kim, J. and Mansour, N. N., Direct Numerical Simulation of Turbulent Channel Flow up to $Re_\tau = 590$, *Physics of Fluids*, 1999, 11(4), 943–945.

[59] Vreman, A. W. and Kuerten, J. G. M., Statistics of Spatial Derivatives of Velocity and Pressure in Turbulent Channel Flow, *Physics of Fluids*, 2014, 26(8), 085103–1/29.

[60] Menter, F. R., Improved Two-Equation $k - \omega$ Turbulence Models for Aerodynamic Flows, NASA Technical Memorandum 103975, 1992.

[61] A.Yoshizawa, Statistical Theory for Compressible Turbulent Shear Flows, with the Application to Subgrid Modeling, *Physics of Fluids*, 1986, 29(7), 2152–2164.

[62] Abbà, A., Bonaventura, L., Nini, M. and Restelli, M., Dynamic Models for Large Eddy Simulation of Compressible Flows with a High Order DG Method, *Computers & Fluids*, 2015, 122, 209–222.